J. Fluid Mech. (1993), *vol.* 255, *pp.* 473–502
Copyright © 1993 Cambridge University Press

Instability of a viscoelastic fluid between rotating parallel disks: analysis for the Oldroyd-B fluid

By ALPARSLAN ÖZTEKIN AND ROBERT A. BROWN
Department of Chemical Engineering, Massachusetts Institute of Technology, Cambridge, MA 02139, USA

(Received 21 January 1993 and in revised form 19 April 1993)

The stability of the viscometric motion of a viscoelastic fluid held between rotating parallel disks with large radii to small-amplitude perturbations is studied for the Oldroyd-B constitutive model. The disturbances are assumed to be radially localized and are expressed in Fourier form so that a separable eigenvalue problem results; these disturbances describe either axisymmetric or spiral vortices, depending on whether the most dangerous disturbance has zero or non-zero azimuthal wavenumber, respectively. The critical value of the dimensionless radius R^* for the onset of the instability is computed as a function of the Deborah number De, a dimensionless time constant of the fluid, the azimuthal and radial wavenumbers, and the ratio of the viscosities of the solvent to the polymer solution. Calculations meant to match the experiments of McKinley *et al.* (1991) for a Boger fluid show that the most dangerous instabilities are spiral vortices with positive and negative angle that start at the same critical radius and travel outward and inward toward the centre of the disk; the axisymmetric mode also becomes unstable at only slightly greater values of R^*, or De for fixed R^*. The predicted dependence of the value of De for a fixed R^* on the gap between the disks agrees quantitatively with the measurements of McKinley *et al.*, when the longest relaxation time for the fluid at the shear rate corresponding to the maximum value of R^* is used to define the time constant in the Oldroyd-B model.

1. Introduction

The motion generated by rotating one of two parallel disks of radius R is one of the most studied flows in fluid mechanics, as it is the basis for rheological measurements of the viscosity and normal stresses in non-Newtonian liquids (Bird, Armstrong & Hassager 1987*a*). The analysis of these measurements assumes that the steady-state viscometric motion

$$(\hat{u}_r, \hat{u}_\theta, \hat{u}_z) = (0, \Omega\hat{r}(1-z/H), 0), \tag{1}$$

is established, where Ω is the rotation rate of the lower disk (the top disk is stationary), H is the spacing between the disks, and the velocity field is expressed in the cylindrical coordinate system shown in figure 1(*a*).

Typically, this approximation is valid as long as edge effects can be ignored, i.e. $H/R \ll 1$, and inertial effects are small enough that secondary motions are unimportant (Griffiths, Jones & Walters 1969; Hill 1972). An additional condition is that the flow does not become unstable by mechanisms caused by the non-Newtonian nature of the fluid. It is this type of instability that is the subject of this paper.

A transition to time-dependent behaviour was first seen by Jackson, Walters & Williams (1984) in experiments with a Boger fluid in a parallel-plate rheometer†. They

† Boger fluids are highly elastic polymer solutions composed of a high-molecular-weight polymer dissolved in an almost Newtonian solvent with high viscosity. The viscosity of the fluid remains

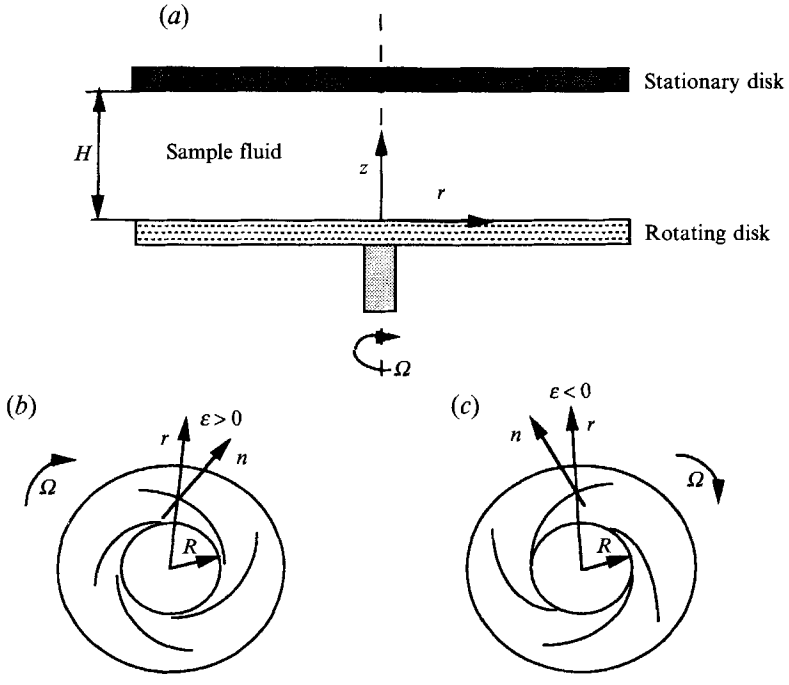

FIGURE 1. (*a*) Prototype parallel-plate configuration, and Ekman spirals orienting at (*b*) a positive angle and (*c*) a negative angle.

observed that at high shear rates, the torque and normal force exerted by the fluid increased steadily over a period of 20 minutes. The increase in torque resulted in an increase in the apparent viscosity of the fluid, hence they coined the expression shear-thickening or anti-thixotropic transition to describe this behaviour and discussed this transition as a rheological change in the fluid. Similar behaviour was observed for other Boger fluids by Binnington & Boger (1986), Laun & Hingmann (1990) and Steiert & Wolff (1990).

Magda & Larson (1988) were the first to suggest that the anti-thixotropic behaviour observed in rotating rheometers for Boger fluids is associated with a flow transition and suggested that, above a critical shear rate, the simple shear flow (1) becomes unstable to a more complicated motion. Magda & Larson used a number of different Boger fluids to vary the elasticity of the fluid and determined the critical shear rate for the instability in both parallel-plate and cone-and-plate devices. In the parallel-plate experiments, they noted that the critical shear rate decreased with increasing elasticity and increased with decreasing the gap between the plates.

McKinley *et al.* (1991) set out convincing results of the presence of a viscoelastic flow instability in experiments using a Boger fluid made by dissolving polyisobutylene (PIB) in a polybutene/tetradecane (PB/C14) solvent. We describe their results for the parallel-plate geometry in some detail because these measurements will be the basis for comparison with the stability analysis presented in this paper. The (PIB/PB/C14) Boger fluid used in these experiments has been well characterized rheologically by Quinzani *et al.* (1990), who showed that the dependence of the viscosity and normal stress on shear rate was only modelled precisely by nonlinear differential constitutive

almost constant, while the first normal stress coefficient of the fluid decreases with increasing shear rate. Various Boger fluids have been used in all the measurements of the viscoelastic instability discussed here.

equations and by a spectrum of relaxation times determined from linear viscoelastic measurements. The longest relaxation time for the fluid can be defined in terms of the zero-shear-rate properties of the fluid as

$$\lambda_0 \equiv \frac{\Psi_{10}}{2(\eta_0 - \eta_s)} = 0.794 \text{ s}, \tag{2}$$

where Ψ_{10} is the zero-shear-rate value of the first normal stress coefficient, η_0 is the zero-shear-rate viscosity and η_s is the viscosity of the PB/C14 solvent.

McKinley *et al.* performed two crucial sets of experiments. In the first, they used a commercial parallel-plate rheometer (Rheometrics RMS-800) to detect the onset of the instability as a function of the rotation rate of the disk and reported the results as a function of the Deborah (De_0) and Weissenberg (We_0) numbers, defined as

$$De_0 \equiv \lambda_0 \Omega \quad \text{and} \quad We_0 \equiv \lambda_0 \Omega R^*, \tag{3}$$

where $R^* \equiv R/H$ is the dimensionless radius or aspect ratio. Here the Deborah number is a ratio of the relaxation time of the fluid to the timescale (Ω^{-1}) for the fluid in the shear flow; the Weissenberg number is the product of the relaxation time and the characteristic shear rate $\Omega R/H$. Time-dependent measurements of the torque and normal force were used to detect the critical value of De for the onset of the instability and to follow its evolution with De. These experiments documented that the instability is described as an initially subcritical Hopf bifurcation, i.e. the unstable transition to a time-dependent flow which restabilizes at a finite-amplitude state. Power spectra of the shear stress of the finite-amplitude states had several unidentifiable peaks among a background of broadband noise and are indicative of the presence of a number of unstable modes in the system. The onset of the instability also was observed by the exponential growth of the normal stress in the fluid for short times – only on the order of 100 s – before nonlinear terms begin to dominate the dynamics. This timescale is much shorter than the transients reported by others.

Perhaps the most convincing evidence for a flow transition was gathered by McKinley *et al.* by flow visualizations of the instability in a larger-scale parallel-plate device. Frames from the video of the onset of the instability using the PIB/PB/C14 Boger fluid are shown as Plate 1 in McKinley *et al.* (1991); their description of the evolution is reproduced here. When the Deborah number for the flow exceeds the critical value for onset, the flow is no longer purely azimuthal, but begins to develop a banded radial structure composed of many roll cells that are approximately axisymmetric and that appear to have a nearly constant radial wavelength which is roughly equal to the separation between the plates H. The cells are not steady in time, but increase in intensity and propagate both radially outwards from the centre of the disks and radially inward from the outer edge; these travelling waves are clearly shown in the video frames referenced above. The structure changes after the two sets of roll cells meet near the middle of the disk; the flow is then composed of irregularly spaced, slightly non-axisymmetric cells that spiral both inwards and outwards.

The linear stability analysis described in this paper is aimed at partially describing the observations of McKinley *et al.* (1991). We analyse the stability of the viscometric motion (1) to small-amplitude, radially localized disturbances at the position $\hat{r} \equiv R$ that can be represented in Fourier form and which lead to a separable eigenvalue problem in linear stability analysis. This approximation is formally equivalent to expanding the dimensionless radial coordinate ($\hat{r}/H$) as $\hat{r} \equiv H(R^* + \delta\xi)$, where $\xi \equiv O(1)$ is the dimensionless radial coordinate and δ is a small parameter, and keeping only the leading-order terms in ϵ. In the cylindrical coordinate system shown in figure 1(*a*),

the disturbances have the form $f(z)\exp(i\hat{\alpha}\hat{r}+im\theta+\hat{\sigma}\hat{t})$, where $\hat{\alpha}$ is the dimensional radial wavenumber, m is an integer constant, m/R corresponds to the azimuthal wavenumber, and $\hat{\sigma}$ is the dimensional growth rate of the disturbance. Axisymmetric disturbances are denoted by $m=0$ and describe radially nested vortices; non-axisymmetric disturbances have $m \neq 0$ and correspond to spiral vortices, as shown in figures 1(*b*) and 1(*c*). The angle of the spiral vortices at $R \gg H$ can be approximated as

$$\epsilon \equiv \arctan\left(\frac{1}{\hat{r}}\frac{\mathrm{d}\hat{r}}{\mathrm{d}\theta}\right) = \arctan\left(\frac{m}{\hat{\alpha}R}\right), \tag{4}$$

as measured from the radial direction. Negative values of ϵ describe right-handed spirals. This analysis is motivated by the successful description of the onset of inertial instability near a rotating disk in a Newtonian fluid by disturbances represented in the same form (Malik, Wilkinson & Orszag 1981; Malik 1986; Öztekin, Bornside & Brown 1993).

The analysis reported here is carried out for the Oldroyd-B constitutive equation, which is based on the micromechanical model of a solution of Hookean dumbbells dissolved in a Newtonian solvent. The Oldroyd-B model is written in dimensional form as

$$\boldsymbol{\tau}+\lambda_0\boldsymbol{\tau}_{(1)} = \eta_0(\dot{\boldsymbol{\gamma}}+\lambda_2\dot{\boldsymbol{\gamma}}_{(1)}), \tag{5}$$

where $\boldsymbol{\tau}$ is the stress tensor, $\dot{\boldsymbol{\gamma}} \equiv (\boldsymbol{\nabla u}+\boldsymbol{\nabla u}^T)$ is the rate-of-strain tensor and $\boldsymbol{\tau}_{(1)}$ is the upper-convected time derivative. The total viscosity of the fluid η_0 has contributions from the solvent η_s and the polymer η_p and is decomposed as $\eta_0 \equiv \eta_s+\eta_p$. The single relaxation time for the fluid is λ_0 and the retardation time is defined as $\lambda_2 \equiv \lambda_0\eta_s/\eta_0$. The Oldroyd-B model predicts a constant viscosity η_0 and a constant first normal stress coefficient. This last prediction does not agree with the behaviour of Boger fluids at high shear rates where the instability is seen. For comparison with experiments we interpret the relaxation time in the Oldroyd-B model λ_0 in terms of the shear-rate-dependent rheological properties of the Boger fluid used by McKinley *et al.* (1991) as

$$\lambda_{10}(\dot{\gamma}) = \frac{\Psi_1(\dot{\gamma})}{2(\eta(\dot{\gamma})-\eta_s)}, \tag{6}$$

where $\dot{\gamma}$ is the shear rate. Shear-rate-dependent values of the Deborah ($De(\dot{\gamma})$) and Weissenberg ($We(\dot{\gamma})$) numbers are defined by replacing λ_0 with $\lambda_{10}(\dot{\gamma})$ in (3). McKinley *et al.* (1991) interpreted their experimental results for the onset of the instability in terms of $De(\dot{\gamma})$ and $We(\dot{\gamma})$ and showed that the value of $De(\dot{\gamma})$ for onset decreased monotonically with increasing $We(\dot{\gamma})$ by increasing the aspect ratio of the gap between the disks, $R^* \equiv R/H$. As described in §5, this behaviour is predicted by the analysis presented here.

The mechanism for the viscoelastic instability described here is related closely to the instability analysed first by Larson, Shaqfeh & Muller (1990) in the Taylor–Couette geometry. Here a purely elastic instability arises from the interaction of the radially varying azimuthal flow and the extensional component of the disturbance in the radial direction in the flow with curved streamlines. The instability is oscillatory, not steady as is the case for the Newtonian flow. Northey, Armstrong & Brown (1990; also see Northey, Armstrong & Brown 1992) used numerical solution of the full equations for the upper-convected Maxwell model to demonstrate that the nonlinear states correspond to radial travelling waves that emanate from the inner cylinder and move outward. They also showed that the number of cells nested radially in the gap increases

with increasing gap; for very wide gaps the picture is reminiscent of the structure for the parallel-plate geometry that is described above. Shaqfeh, Muller & Larson (1992) solved the full linear stability problem and reached the same conclusion. An extensive review of the Taylor–Couette and other viscoelastic flow instabilities is given by Larson (1992).

The only previous analysis of viscoelastic instability in parallel-plate rotating flow is the calculation of Phan-Thien (1985) for the stability of the base flow of an Oldroyd-B fluid to disturbances that can be written in the similarity form appropriate for unbounded disks. Phan-Thien predicted an instability to disturbances of this form at the critical Deborah number

$$De_0^{(PT)} = \frac{\pi}{[(1-\beta)(5-2\beta)]^{\frac{1}{2}}}, \tag{7}$$

where $\beta \equiv \eta_s/\eta_0$ is the ratio of the solvent viscosity to the total viscosity of the polymer solution. Because the disturbance in Phan-Thien's analysis is written in similarity form, the flow must be uniform in the radial direction and cannot model the roll cells seen in the experiments of McKinley *et al.* (1991). Phan-Thien's analysis predicts instability to a steady-state mode, not the oscillatory instability seen in the experiments. Also, the value $De_0^{(PT)}$ for the onset of instability predicted by Phan-Thien's is independent of the gap and is predicted to occur at a value of $De(\dot{\gamma})$ greater than the value seen in the experiments of McKinley *et al.* (1991) for any value of R^*; moreover, the experiments show that $De(\dot{\gamma})$ decreases with increasing R^* and hence moves away from the value $De(\dot{\gamma})$ adjusted for the shear-rate-dependence of the relaxation time.

The outline of the paper is as follows. The equations governing the linear stability of radially localized disturbances are described in §2 and the solution method for the associated eigenvalue problem is outlined in §3. Results are described in §§4.1 and 4.2 for the Oldroyd-B ($\eta_s > 0$) and upper-convected Maxwell ($\eta_s = 0$) models, respectively. The predictions are compared in §5 with the experiments of McKinley *et al.* (1991). The mechanism for the instability is discussed in §6 and is shown to be directly related to the mechanism described by Larson *et al.* (1990) for the viscoelastic instability in Taylor–Couette flow.

2. Formulation: governing equations

We consider a viscoelastic fluid contained between two parallel coaxial disks separated by a distance H. The bottom disk is rotated about its vertical axis with angular velocity Ω and the top disk is stationary. The flow is described in the cylindrical coordinate system $(\hat{r}, \theta, \hat{z})$ shown in figure 1(*a*) with $\hat{z} = 0$ positioned on the rotating disk. The inertialess equations governing mass and momentum conservation are

$$\nabla \cdot \hat{\boldsymbol{u}} = 0, \tag{8}$$

$$\nabla \cdot \hat{\boldsymbol{S}} - \nabla \hat{p} + \eta_s \nabla \cdot \dot{\gamma} = 0, \tag{9}$$

where $\hat{\boldsymbol{u}}$ is the velocity vector, $\hat{\boldsymbol{S}}$ is the polymeric contribution to the deviatoric stress tensor and $\hat{p}$ is the pressure. In this formulation the total deviatoric stress tensor τ has been decomposed as $\tau \equiv \hat{\boldsymbol{S}} + \eta_s \dot{\gamma}$. The polymeric contribution to the deviatoric stress tensor is given by the Oldroyd-B model (Bird *et al.* 1987*a*) as

$$\hat{\boldsymbol{S}} + \lambda_{10}\left[\frac{\partial \hat{\boldsymbol{S}}}{\partial \hat{t}} + \hat{\boldsymbol{u}} \cdot \nabla \hat{\boldsymbol{S}} - (\nabla \hat{\boldsymbol{u}})^T \cdot \hat{\boldsymbol{S}} - \hat{\boldsymbol{S}} \cdot \nabla \hat{\boldsymbol{u}}\right] = \eta_p \dot{\gamma}. \tag{10}$$

The boundary conditions on the velocity field $\hat{\boldsymbol{u}}$ are

$$\hat{\boldsymbol{u}}^T(\hat{r},\theta,0,\hat{t}) = (0,\hat{r}\Omega,0), \qquad \hat{\boldsymbol{u}}^T(\hat{r},\theta,H,\hat{t}) = (0,0,0). \tag{11a, b}$$

In the absence of fluid inertia, the purely azimuthal, steady-state viscometric flow is given by the velocity field

$$\hat{\boldsymbol{u}}_0^T = (0,\Omega\hat{r}(1-\hat{z}/H),0). \tag{12}$$

For the Oldroyd-B model the corresponding stress and pressure field, $\hat{\boldsymbol{S}} = \boldsymbol{S}_0$ and $\hat{p} = p_0$, are given in component form as

$$\begin{aligned} &S_{0rr} = S_{0r\theta} = S_{0rz} = S_{0zz} = 0; \quad S_{0\theta z} = -\eta_p\Omega\hat{r}(\hat{r}/H); \quad S_{0\theta\theta} = 2\eta_p\lambda_{10}\Omega^2\hat{r}^2/H^2; \\ &p_0 = -\eta_p\lambda_{10}\Omega^2\hat{r}^2/H^2. \end{aligned} \tag{13}$$

Equations governing the linear stability of the base flow, are formed for dimensionless variables scaled with $(H,\Omega^{-1},H\Omega,\eta_0\Omega)$ for (length, time, velocity, stress). The dimensionless cylindrical coordinates are denoted by (r,θ,z) and the dimensionless time by t. The disturbances to the velocity, pressure, and stress fields are written as

$$\begin{bmatrix} \tilde{u}_r \\ \tilde{u}_\theta \\ \tilde{u}_z \\ \tilde{p} \\ \tilde{S}_{rr} \\ \tilde{S}_{r\theta} \\ \tilde{S}_{rz} \\ \tilde{S}_{\theta\theta} \\ \tilde{S}_{\theta z} \\ \tilde{S}_{zz} \end{bmatrix} (r,\theta,z,t) = \begin{bmatrix} 0 \\ r(1-z) \\ 0 \\ -De(1-\beta)r^2 \\ 0 \\ 0 \\ 0 \\ 2De(1-\beta)r^2 \\ -(1-\beta)r \\ 0 \end{bmatrix} + \begin{bmatrix} u_r \\ u_\theta \\ u_z \\ p \\ S_{rr} \\ S_{r\theta} \\ S_{rz} \\ S_{\theta\theta} \\ S_{\theta z} \\ S_{zz} \end{bmatrix} (r,\theta,z,t), \tag{14}$$

where $(\tilde{u}_r,\tilde{u}_\theta,\tilde{u}_z)$ are the dimensionless (radial, azimuthal, axial) components of the velocity field, $\tilde{p}$ is the pressure, $(\tilde{S}_{rr},\tilde{S}_{r\theta},\tilde{S}_{rz},\tilde{S}_{\theta\theta},\tilde{S}_{\theta z},\tilde{S}_{zz})$ are the components of the contribution to the polymeric stress, (u_r,u_θ,u_z) are the components of the disturbance to the velocity field, p is the disturbance to the pressure, $(S_{rr},S_{r\theta},S_{rz},S_{\theta\theta},S_{\theta z},S_{zz})$ are the disturbances to the polymer contribution to the deviatoric stress. The Deborah number is defined as $De \equiv \lambda_{10}\Omega$.

Substituting (14) into (8)–(11), subtracting the base state, (12) and (13), and retaining only terms that are linear in the disturbance amplitude, yields the dimensionless disturbance equations and boundary conditions. The continuity and momentum equations are

$$\frac{\partial u_r}{\partial r} + \frac{u_r}{r} + \frac{1}{r}\frac{\partial u_\theta}{\partial\theta} + \frac{\partial u_z}{\partial z} = 0, \tag{15}$$

$$\frac{1}{r}\frac{\partial}{\partial r}(rS_{rr}) + \frac{1}{r}\frac{\partial S_{r\theta}}{\partial\theta} + \frac{\partial S_{rz}}{\partial z} - \frac{S_{\theta\theta}}{r} - \frac{\partial p}{\partial r} + \beta\left(\nabla^2 u_r - \frac{2}{r^2}\frac{\partial u_\theta}{\partial\theta} - \frac{u_r}{r^2}\right) = 0, \tag{16a}$$

$$\frac{\partial S_{r\theta}}{\partial r} + \frac{1}{r}\frac{\partial S_{\theta\theta}}{\partial\theta} + \frac{\partial S_{\theta z}}{\partial z} + 2\frac{S_{r\theta}}{r} - \frac{1}{r}\frac{\partial p}{\partial\theta} + \beta\left(\nabla^2 u_\theta + \frac{2}{r^2}\frac{\partial u_r}{\partial\theta} - \frac{u_\theta}{r^2}\right) = 0, \tag{16b}$$

$$\frac{1}{r}\frac{\partial}{\partial r}(rS_{rz}) + \frac{1}{r}\frac{\partial S_{\theta z}}{\partial\theta} + \frac{\partial S_{zz}}{\partial z} - \frac{\partial p}{\partial z} + \beta\nabla^2 u_z = 0, \tag{16c}$$

where ∇^2 is the Laplacian operator in cylindrical coordinates. The linearized components of the constitutive equations are

$$\mathrm{L}(S_{rr}) = 2\beta_p \frac{\partial u_r}{\partial r}, \tag{17a}$$

$$\mathrm{L}(S_{r\theta}) + De\, r S_{rz} - 2\beta_p De\, r \frac{\partial u_r}{\partial \theta} + \beta_p De\, r \frac{\partial u_r}{\partial z} = \beta_p \left(\frac{1}{r}\frac{\partial u_r}{\partial \theta} - \frac{u_\theta}{r} + \frac{\partial u_\theta}{\partial r} \right), \tag{17b}$$

$$\mathrm{L}(S_{rz}) + \beta_p De \frac{\partial u_r}{\partial \theta} = \beta_p \left(\frac{\partial u_r}{\partial z} + \frac{\partial u_z}{\partial r} \right), \tag{17c}$$

$$\mathrm{L}(S_{\theta\theta}) + 2\, De\, r S_{\theta z} - 4\beta_p De^2 r \frac{\partial u_\theta}{\partial \theta} + 2\beta_p De\, r \frac{\partial u_\theta}{\partial z} = \beta_p \left(\frac{1}{r}\frac{\partial u_\theta}{\partial \theta} + \frac{u_r}{r} \right), \tag{17d}$$

$$\mathrm{L}(S_{\theta z}) + De\, r S_{zz} - 2\beta_p De^2 r \frac{\partial u_z}{\partial \theta} + \beta_p De\, r \frac{\partial u_z}{\partial z} + \beta_p De \frac{\partial u_\theta}{\partial \theta} = \beta_p \left(\frac{1}{r}\frac{\partial u_z}{\partial \theta} + \frac{\partial u_\theta}{\partial z} \right), \tag{17e}$$

$$\mathrm{L}(S_{zz}) + 2\beta_p De \frac{\partial u_z}{\partial \theta} = 2\beta_p \frac{\partial u_z}{\partial z}, \tag{17f}$$

where $\mathrm{L}(\cdot) \equiv (1 + De\,\partial/\partial t + De\, r(1-z)\,\partial/\partial\theta)$ and $\beta_p \equiv (1-\beta)$. The boundary conditions for the disturbance velocity are

$$\boldsymbol{u}^T(r, \theta, z, t) = (0, 0, 0) \quad \text{at} \quad z = 0 \text{ and } z = 1. \tag{18}$$

As written in (16) and (17), the linear disturbance equations are not separable. We follow Malik *et al.* (1981), Malik (1986) and Öztekin *et al.* (1993) and restrict the analysis to disturbances that are localized in r. The spatial dependence of each disturbance equation can be separated, if the disturbance is written in the Fourier form $\exp(\mathrm{i}\alpha r + \mathrm{i}m\theta + \sigma t)$, where α is the dimensionless radial wavenumber of the disturbance, m is an integer (which can be positive, zero, or negative), and σ is the dimensionless temporal eigenvalue (which can be complex). Substituting this form into (15)–(18) and eliminating the pressure and stress components from (16*a–c*) using (15) and (17*a–f*) yields

$$\sum_{n=0}^{4} P^n \left(\sum_{k=0}^{4} a_{nk}(\alpha, m, De, R^*, \beta)\, \mathrm{D}^k W + \sum_{j=0}^{2} b_{nj}(\alpha, m, De, R^*, \beta)\, \mathrm{D}^j \omega \right) = 0, \tag{19}$$

$$\sum_{n=0}^{4} P^n \left(\sum_{k=0}^{2} c_{nk}(\alpha, m, De, R^*, \beta)\, \mathrm{D}^k \omega + \sum_{j=0}^{2} d_{nj}(\alpha, m, De, R^*, \beta)\, \mathrm{D}^j W \right) = 0, \tag{20}$$

where $\mathrm{D} \equiv \mathrm{d}/\mathrm{d}z$, $P \equiv [1 + De\,\sigma + \mathrm{i}\, De\, m(1-z)]$, $W(z)$ is the amplitude of the disturbances to the vertical velocity, $\omega(z) \equiv \mathrm{i}\alpha V(z) - \mathrm{i}mU(z)/R^* \equiv \bar{\omega}(z) - V(z)/R^*$, where $\bar{\omega}(z)$ is the amplitude of the disturbance to the vertical vorticity and $U(z)$ and $V(z)$ are the amplitudes of the disturbances to the radial and azimuthal velocity, respectively. It is obvious from this definition that $\omega(z)$ approximates the amplitude of the disturbance to the vertical vorticity for large values of R^*. Details of the coefficients $a_{nj}(\alpha, m, De, R^*, \beta)$, $b_{nj}(\alpha, m, De, R^*, \beta)$, $c_{nj}(\alpha, m, De, R^*, \beta)$ and $d_{nj}(\alpha, m, De, R^*, \beta)$ are available from the authors. In this form $R^* \equiv R/H$ is the dimensionless radial location for the localized disturbance. The boundary conditions on the linear stability problem are

$$W(0) = DW(0) = \omega(0) = 0 \tag{21a–c}$$

and

$$W(1) = DW(1) = \omega(1) = 0. \tag{21d–f}$$

3. Numerical solution

Equations (19) and (20) describe an eigenvalue problem for the growth rate σ and the eigenfunction, composed of $W(z)$ and $\omega(z)$, as a function of the spatial wavenumbers (α, m), the dimensionless radial distance R^* and the parameters De and β. The eigenvalue problem is solved by discretization using Chebyshev polynomials.

The components of the eigenfunction are expanded in truncated series of Chebyshev polynomials. These expansions are simplified by transforming the computational domain $0 \leqslant z \leqslant 1$ to $\zeta \equiv -2z+1$, so that the new variable ζ satisfies $-1 \leqslant \zeta \leqslant +1$. The transformed eigenvalue problems is solved using the Galerkin technique developed by Zebib (1987), in which the highest derivatives of the components of the eigenfunction corresponding to the disturbances in the axial velocity and $\omega(\zeta)$ are approximated by truncated sums of Chebyshev polynomials of the form

$$\mathrm{D}^4 W(\zeta) = \sum_{j=0}^{N} A_j T_j(\zeta), \qquad \mathrm{D}^2 \omega(\zeta) = \sum_{j=0}^{N} B_j T_j(\zeta), \tag{22a, b}$$

where T_j is the jth Chebyshev polynomial and the coefficients $\{A_j, B_j\}$ are computed as the solution of the algebraic eigenvalue problem. Representations of lower-order derivatives are computed by integrating (22) and using standard properties of Chebyshev polynomials. The Galerkin procedure described by Zebib (1987) reduces the problem to a matrix eigenvalue problem

$$(\sigma^4 \boldsymbol{A} + \sigma^3 \boldsymbol{B} + \sigma^2 \boldsymbol{C} + \sigma \boldsymbol{D} + \boldsymbol{E})\, \boldsymbol{x}_1 = \boldsymbol{0}, \tag{23}$$

where σ is the temporal eigenvalue, $\boldsymbol{x}_1 \in \Re^{2(N+1)}$ are the components of the discretized eigenvector and the elements of the square matrices $(\boldsymbol{A}, \boldsymbol{B}, \boldsymbol{C}, \boldsymbol{D}, \mathrm{E})$, each in $\Re^{2(N+1)\times 2(N+1)}$, depend on $(\alpha, m, De, R^*, \beta)$. The leading-order term $(\sigma^4 \boldsymbol{A})$ in (23) arises from the viscous contribution in (16) and is proportional to the viscosity ratio $\beta \equiv \eta_s/\eta_0$. Because the matrix $\boldsymbol{A}$ is non-singular for the Oldroyd-B model ($\beta \neq 0$), the decomposition

$$\sigma \boldsymbol{I} \boldsymbol{x}_1 = \boldsymbol{I} \boldsymbol{x}_2, \quad \sigma \boldsymbol{I} \boldsymbol{x}_2 = \boldsymbol{I} \boldsymbol{x}_3, \quad \sigma \boldsymbol{I} \boldsymbol{x}_3 = \boldsymbol{I} \boldsymbol{x}_4, \tag{24a–c}$$

where $\boldsymbol{I}$ is the identity matrix in $\Re^{2(N+1)\times 2(N+1)}$, transforms (23) to the generalized eigenvalue problem

$$(\sigma \boldsymbol{E} + \boldsymbol{F})\, \boldsymbol{s} = \boldsymbol{0}, \tag{25}$$

where $\boldsymbol{E} \in \Re^{8(N+1)\times 8(N+1)}$, $\boldsymbol{F} \in \Re^{8(N+1)\times 8(N+1)}$ and $\boldsymbol{s} = [\boldsymbol{x}_1, \boldsymbol{x}_2, \boldsymbol{x}_3, \boldsymbol{x}_4]^T$.

The stability analysis of the upper-convected Maxwell fluid ($\beta = 0$) requires special treatment. The vanishing of the leading-order term in (23) in this limit leaves

$$(\sigma^3 \boldsymbol{B} + \sigma^2 \boldsymbol{C} + \sigma \boldsymbol{D} + \boldsymbol{E})\, \boldsymbol{x}_1 = \boldsymbol{0}, \tag{26}$$

where $\boldsymbol{B}$ is non-singular. Equation (26) is reduced by the decomposition

$$\sigma \boldsymbol{I} \boldsymbol{x}_1 = \boldsymbol{I} \boldsymbol{y}_1, \quad \sigma \boldsymbol{I} \boldsymbol{y}_1 = \boldsymbol{I} \boldsymbol{y}_2, \tag{27a, b}$$

to the generalized eigenvalue problem

$$(\sigma \boldsymbol{H} + \boldsymbol{G})\, \boldsymbol{s}_1 = \boldsymbol{0}, \tag{28}$$

where $\boldsymbol{H} \in \Re^{6(N+1)\times 6(N+1)}$, $\boldsymbol{G} \in \Re^{6(N+1)\times 6(N+1)}$, and $\boldsymbol{s}_1 = [\boldsymbol{x}_1, \boldsymbol{y}_1, \boldsymbol{y}_2]^T$. The eigenvectors and eigenvalues of the algebraic eigenproblems, (25) and (28), are computed using the algorithm available as DGVCCG in the IMSL library.

The stability of the viscometric flow is characterized for given De and m by neutral stability curves of $R^* = R^*(\alpha)$ along which $\mathrm{Re}(\sigma) = 0$. These curves are determined by

computing the growth rate σ for fixed values of (α, m, De) and several values of R^* and using bisection to determine the critical value $R^*(\alpha)$. For each instability mode, a search in radial wavenumber α is used to determine the most dangerous disturbance defined as the one corresponding to the minimum value of R^*. These searches are carried out to one part in 10^6.

4. Results

4.1. *Oldroyd-B model*

Calculations of the stability of an Oldroyd-B model are described for the solvent viscosity ratio of $\beta = 0.59$, the value for the PIB/PB/C14 Boger fluid used by McKinley *et al.* (1991), and for values of the viscosity ratio in the range $0 \leqslant \beta \leqslant 1$. Calculations are reported first for the axisymmetric mode ($m = 0$), followed by calculations for m in the range $-10 \leqslant m \leqslant 10$.

4.1.1. *Axisymmetric instability: $m = 0$*

The accuracy of the Galerkin/Chebyshev approximation for the eigenvalue problem was tested by checking the spectral convergence of the eigenvalues with smallest real part. The real and imaginary parts of the least-stable axisymmetric ($m = 0$) eigenvalues are plotted in figure 2 as a function of the number of polynomials in the expansions (22) for Deborah numbers of 1, 2, 3, and 5 and for the parameter values $R^* = 5$, $\beta = 0.59$, and $\alpha = 3.5$. For each value of De, both the real and imaginary parts of the eigenvalue convergence for values of N as small as five.

The neutral stability curves $R^* = R^*(\alpha)$ computed for axisymmetric disturbances ($m = 0$) and $\beta = 0.59$ are shown in figure 3 for $1 \leqslant De \leqslant 5$. For any value of De, there is a critical value $R^* = R^*_{crit}(\alpha_{crit})$ that corresponds to the minimum radius for the onset of the instability. For $R^* < R^*_{crit}(\alpha_{crit})$ the viscometric flow is stable for all values of the radial wavenumber α, whereas for $R^* > R^*_{crit}(\alpha_{crit})$ the flow is unstable to disturbances in some range of α. Monotonically increasing De decreases the curves $R^* = R^*(\alpha)$, making the flow more unstable in the sense that the instability begins at a smaller value of the dimensionless radius. The value of the radial wavenumber changes little with De. The most dangerous radial wavenumber remains at $\alpha_{crit} \approx 3.2$ which corresponds to the wavelength being approximately twice the gap spacing $2H$ in dimensional units.

The axial variation in the coordinate z of the real and imaginary parts of the vertical velocity $W(z)$, $\omega(z) \equiv i\alpha V(z) - imU(z)/R^*$ and the components of the polymer part of the deviatoric stress are shown in figure 4 as computed for the critical values $R^* = R^*_{crit}(\alpha_{crit})$ for $De = 3$ and $\beta = 0.59$. The disturbance in the vertical velocity and $\omega(z)$ are symmetric about the midplane defined by $z = 0.5$, as shown in figures 4(*a*) and 4(*b*), with a maximum amplitude at the midplane and zero at the disks. The stress components are either symmetric ($S_{r\theta}, S_{rz}$) or antisymmetric ($S_{\theta\theta}, S_{\theta z}, S_{zz}, S_{rr}$) about the midplane $z = 0.5$. This eigenfunction structure is not comparable to that predicted by Shaqfeh *et al.* (1992) for the Taylor–Couette flow. Here the disturbances are radially and azimuthally periodic and the amplitudes vary in the axial direction, whereas for Taylor–Couette flow, the disturbances are axially and azimuthally periodic but the amplitudes vary radially. The most dangerous mode predicted for Taylor–Couette flow has more than one cell in the radial direction, but the velocity eigenfunction for the flow between rotating disks has only one cell between the plates.

The instabilities defined by the neutral curves shown in figures 3 and 4 correspond to travelling waves with positive wave speeds $c \equiv -\mathrm{Im}(\sigma)/\alpha$, i.e. to waves that travel

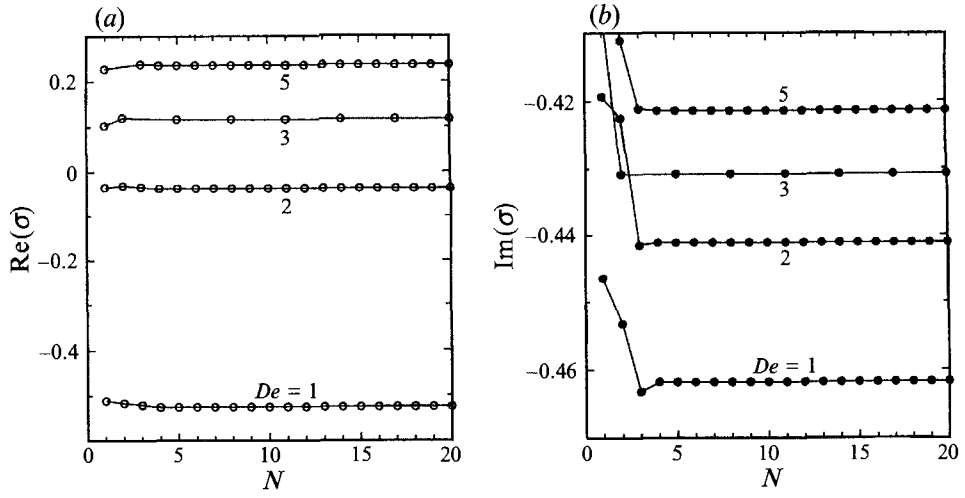

FIGURE 2. (*a*) The real and (*b*) imaginary parts of the least stable axisymmetric ($m = 0$) eigenvalues as functions of the number of polynomials in the expansion N for $De = 1$, 2, 3 and 5, and for $R^* = 5$, $\beta = 0.59$ and $\alpha = 3.5$.

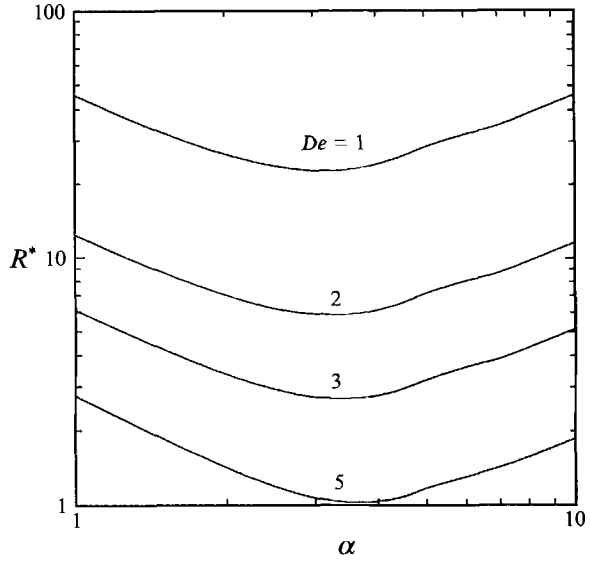

FIGURE 3. The neutral stability curves $R^* = R^*(\alpha)$ computed for axisymmetric disturbances ($m = 0$), $\beta = 0.59$ and for $De = 1$, 2, 3 and 5.

radially *outward*. The dependence of the critical wave speed c_{crit} and wavenumber α_{crit} on De is shown in figure 5 for $\beta = 0.59$. The critical wavenumber α_{crit} increases slightly with increasing De until it reaches a maximum at approximately $De = 6$, as shown in figure 5(*a*). The wave speed depends monotonically on De and increases toward zero at large De. Hence, the disturbances slow with increasing De until they become approximately stationary as De approaches 10.

The travelling wave form of the disturbance and the shape of the neutral stability curves gives a picture of the instability that is consistent with the observations of McKinley *et al.* (1991). For a parallel-plate apparatus with given aspect ratio, R/H, the

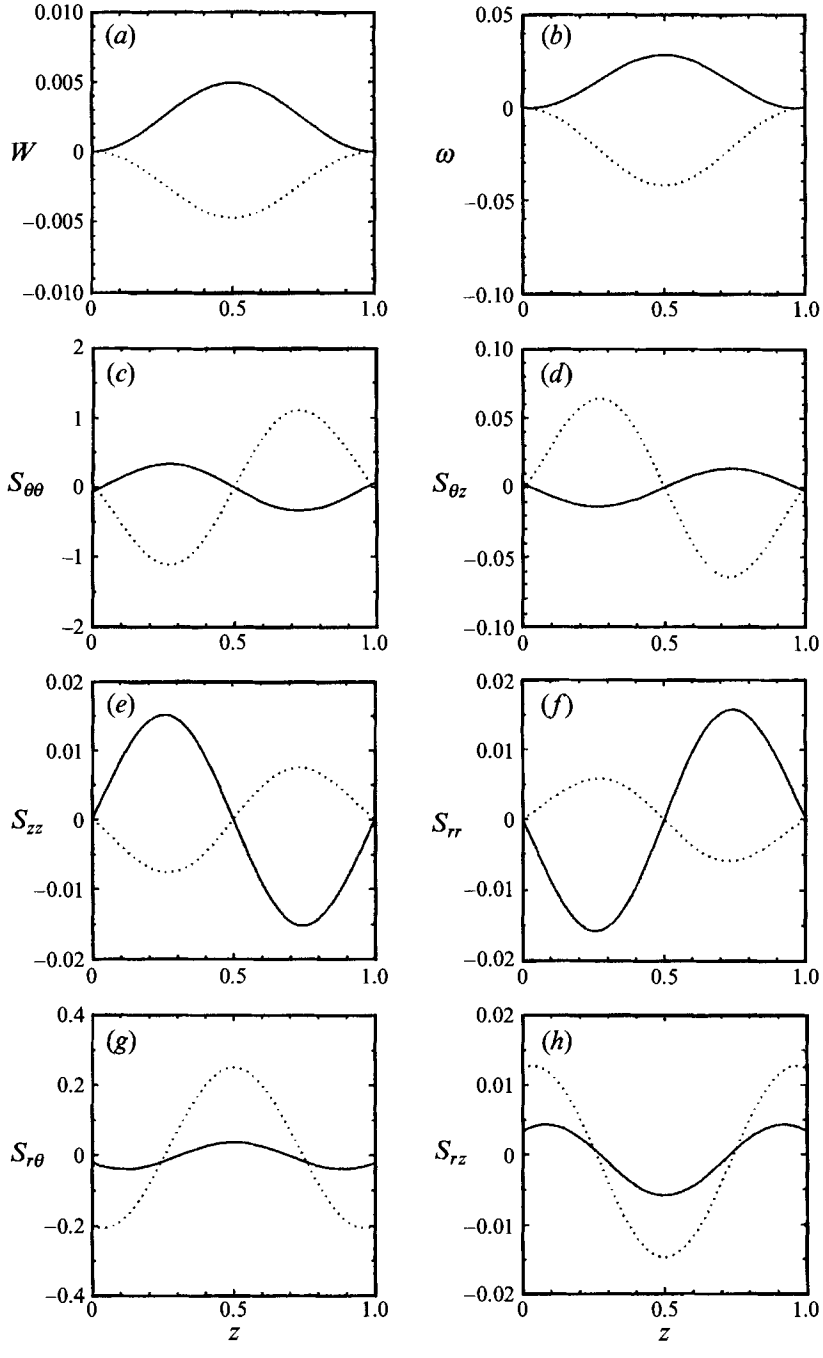

FIGURE 4. Disturbance amplitudes for Boger fluid ($\beta = 0.59$) shown as the plots of the real (solid curve) and imaginary parts (dotted curve) of (*a*) $W(z)$, (*b*) $\omega(z)$, (*c*) $S_{\theta\theta}$, (*d*) $S_{\theta z}$, (*e*) S_{zz}, (*f*) S_{rr}, (*g*) $S_{r\theta}$, and (*h*) S_{rz}. Plots are for the axisymmetric disturbances ($m = 0$), $R^* = 2.70$, $\beta = 0.59$ and $\alpha = 3.5$.

instability is expected to start when the Deborah number is increased above a critical value where $R = R^*_{crit}(\alpha_{crit})H$. For De above this value, travelling axisymmetric vortices are expected to emanate from the critical radius and move radially outward. A more precise comparison between the stability calculations and their observations is

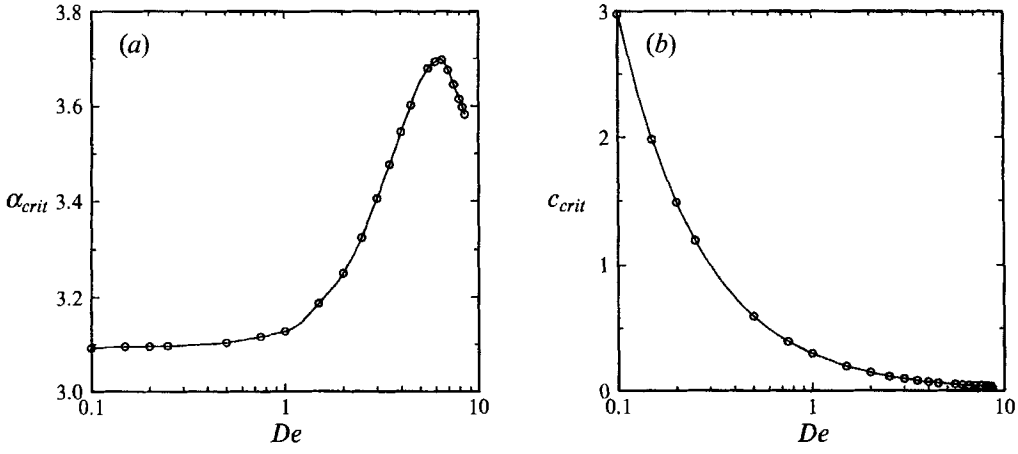

FIGURE 5. (a) The critical wavenumber α_{crit} and (b) wave speed c_{crit} of the axisymmetric disturbances ($m = 0$) as a function of De for $\beta = 0.59$.

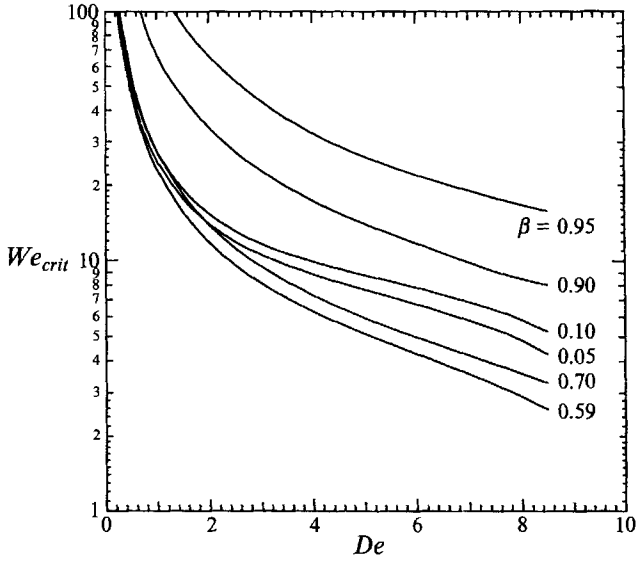

FIGURE 6. The critical Weissenberg number We_{crit} for the onset of the axisymmetric instability as a function of De for a viscosity ratio $0.05 \leqslant \beta \leqslant 0.95$.

reported in §5. Outward-moving radial vortices were also predicted for the Taylor–Couette flow by Northey, Armstrong & Brown (1992) and Shaqfeh *et al.* (1992).

The critical value of the radius $R^* \equiv R^*_{crit}(\alpha_{crit})$ for the onset of the axisymmetric instability is plotted in terms of the Weissenberg number, defined by (3) as $We_{crit} \equiv De\, R^*_{crit}$, in figure 6 for a range of the viscosity ratio $0.05 \leqslant \beta \leqslant 0.95$. For all values of the viscosity ratio We_{crit} is a decreasing function of De, indicating that the critical radius decreases with increasing De. Also We_{crit} approaches infinity as De tends to zero, indicating the stability of the Newtonian inertialess flow. Interestingly, the neutral stability curves for fluids with β in the range $0.05 \leqslant \beta \leqslant 0.7$ are very close for $0 < De < 2$; however, these curves separate for larger De.

Alternatively, the dependence of $We_{crit} \equiv De\, R^*_{crit}$ on β is shown in figure 7 for

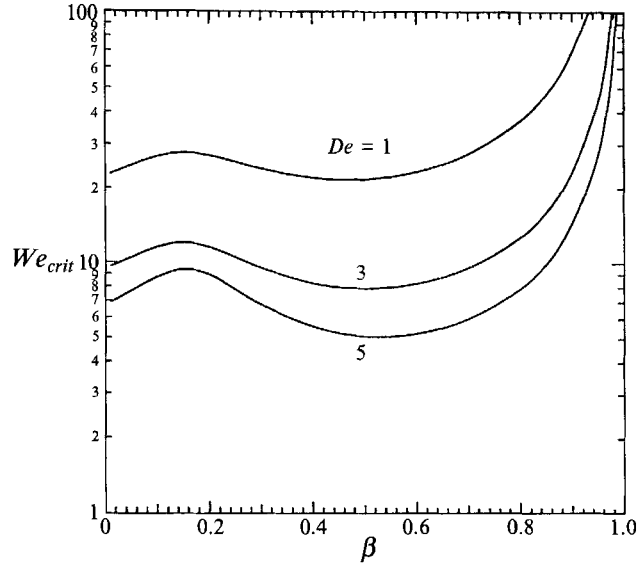

FIGURE 7. The critical Weissenberg number We_{crit} for the onset of the axisymmetric instability as a function of β for $De = 1$, 3 and 5.

various values of De. The results for the UCM model correspond to the limit $\beta \to 0$, which cannot be computed with the solution method used for $\beta > 0$; see the discussion in §3. As $\beta \to 1$ all disturbances are stabilized, i.e. $We_{crit} \to \infty$. The Oldroyd-B model reduces to a Newtonian fluid with viscosity $\eta_0 = \eta_s$ in this limit. Each curve for fixed De has a shallow minimum that corresponds to a most unstable value of the viscosity ratio, i.e. to instability occurring at a smaller radius. This minimum becomes more pronounced with increasing De.

4.1.2. *Non-axisymmetric instability: $m \neq 0$*

Linear stability calculations for non-axisymmetric disturbances ($m \neq 0$) have proven to be more difficult than for the axisymmetric modes. Insight into the difficulty with these calculations is readily gained by calculation of the spectrum of the eigenvalue problem predicted as a function of the polynomial discretization. The spectra are shown in figure 8 for calculations with N between 30 and 60 and for $m = 1$, $\alpha = 3.5$, $R^* = 5$, $\beta = 0.59$ and $De = 3$. Two different types of eigenvalues are found for each discretization, corresponding to continuous and discrete parts of the spectrum of the original problem. Eight branches of what appears to be a continuous spectrum are identifiable with imaginary components that vary between $-m \leqslant \mathrm{Im}(\sigma) \leqslant 0$. Six of these branches connect at points where the real parts are approximately $-1/De$ and the imaginary parts are nearly 0 and $-m$. The real parts of the other branches are smaller than $-1/De$. It appears that the upper branch of the continuous spectrum extends from $-1/De$ to $(-1/De - im)$ as N increases; however, resolution of the associated eigenfunctions requires the use of large N. Discrete eigenvalues also are computed, as shown in figure 8. Increasing the number of polynomials in the discretization from 30 to 60 increases the number of discrete eigenvalues from 13 to 23, with the remaining additional eigenvalues in the algebraic problem adding to the continuous spectrum.

The spectrum shown in figure 8 has similarities to the eigenvalue spectrum for two-dimensional disturbances to inertialess planar Couette flow, which can be computed in

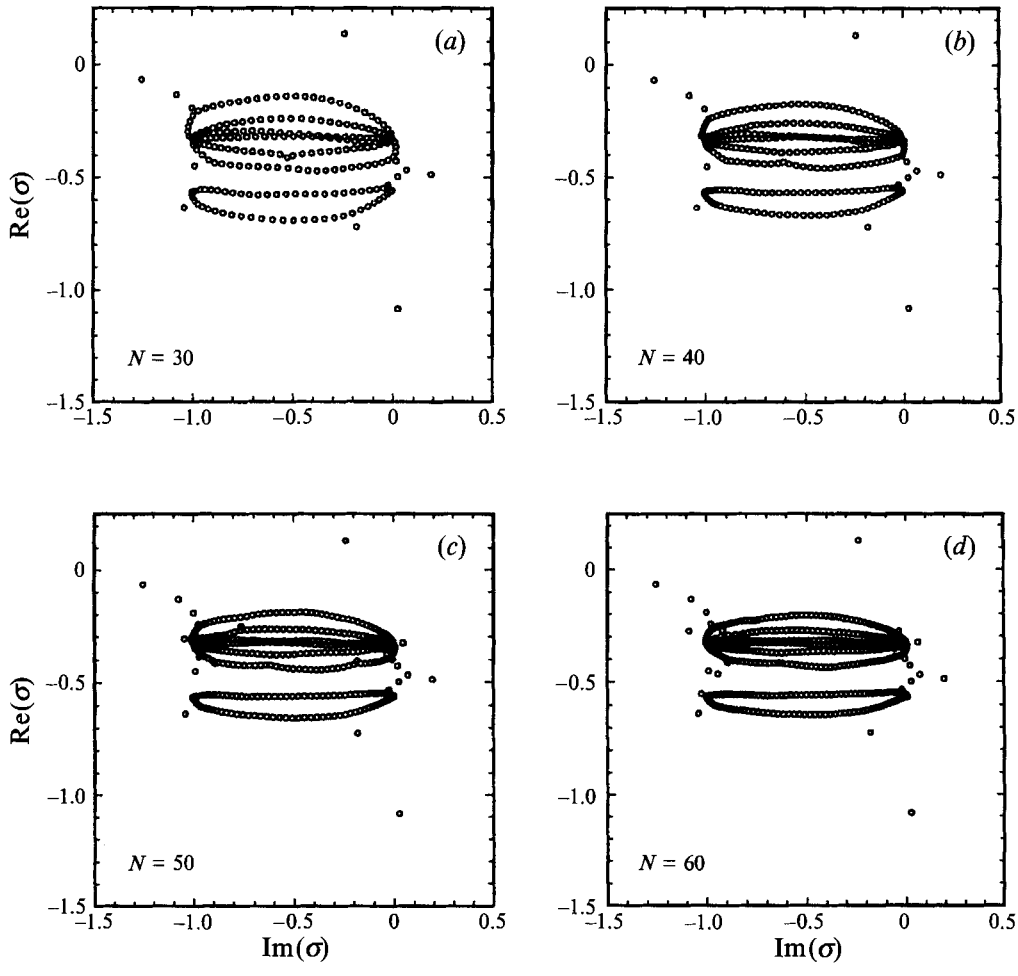

FIGURE 8. The spectra of the algebraic eigenvalue problem computed for $m = 1$, $\alpha = 3.5$, $R^* = 5$, $\beta = 0.59$, $De = 3$, with the discretization using (*a*) $N = 30$, (*b*) 40, (*c*) 50 and (*d*) 60.

closed form for the UCM model (Gorodtsov & Leonov 1967). Gorodtsov & Leonov found both continuous and discrete parts of the spectrum. The continuous spectrum extended from $(-1/De-\alpha i)$ to $(-1/De+\alpha i)$, where α is the spatial wavenumber in the streamwise direction and De is defined based on the width of the gap and the relaxation time for the fluid. The real part of all the eigenvalues in the discrete spectrum was $-1/(2De)$ and so corresponded to the most dangerous disturbance. This flow is never unstable to these disturbances; see Brown *et al.* (1993) for more discussion.

The accuracy of the calculation of the eigenvalues for the rotating disk flow for non-axisymmetric disturbances was tested by repeating calculations with $\alpha = 3.5$, $R^* = 5$, $\beta = 0.59$ and $De = 3$ for a number of values of m and N; these results are shown in figure 9 for $1 \leqslant m \leqslant 3$. The convergence of the continuous part of the spectrum was considerably slower than for the eigenvalues of the discrete spectrum; moreover, disturbances with higher m require higher spectral resolution. The convergence of the most unstable (largest real part) eigenvalue in the discrete spectrum is shown in figures 9(*a*) and 9(*b*), for the real and imaginary parts of the growth rate σ, respectively; good convergence is obtained for $N = 15$, 20 and 35, depending on whether m is 1, 2, or 3, respectively. In contrast, the most unstable eigenvalue of the continuous spectrum does

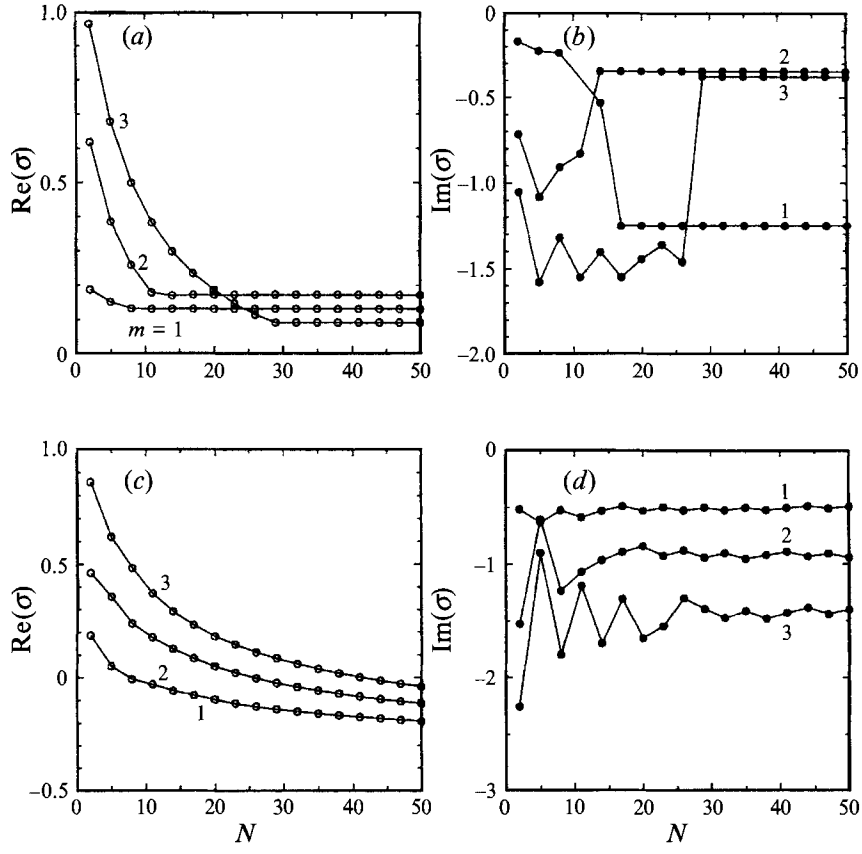

FIGURE 9. The spectral convergence of the least-stable eigenvalues for $\alpha = 3.5$, $R^* = 5$, $\beta = 0.59$, $De = 3$ and $1 \leqslant m \leqslant 3$, shown as plots of (*a*) the real and (*b*) imaginary parts of the most unstable eigenvalue of the discrete spectrum, and (*c*) the real and (*d*) imaginary parts of the most unstable eigenvalue of the continuous spectrum as a function of discretization N.

not converge adequately for N of 50 for any m, as shown by the plots of the real and imaginary parts of this eigenvalue in figures 9(*c*) and 9(*d*). Note that the slopes of the dependence of $\mathrm{Re}(\sigma)$ and $\mathrm{Im}(\sigma)$ on N are very small, indicating that extremely large values of N are needed for accurate computation of these eigenvalues. The real part of this eigenvalue appears to approach $-1/De$ as $N \to \infty$.

It is interesting to note that for small enough N, the least-stable eigenvalue from the continuous spectrum is predicted to be unstable, i.e. $\mathrm{Re}(\sigma) > 0$, and that the value of N needed to remove this numerically induced instability increases with increasing m. This result belies the difficulties with numerical simulation of viscoelastic flows, where fine spatial discretizations are needed for stable calculations. The calculations reported below are based on the value of N for which the most unstable mode in the discrete spectrum is converged to one part in 10^4 and all the algebraic eigenvalues that belong to the continuous part of the spectrum are stable.

As shown in figures 1(*b*) and 1(*c*), non-axisymmetric disturbances correspond to spiral instabilities to the viscometric flow with spiral angle $\epsilon \equiv \arctan(m/\alpha R^*)$ formed by the spiral and the radial vector. Then positive-angle spirals ($\epsilon > 0$) are recovered from disturbances with $m > 0$ and negative-angle spirals ($\epsilon < 0$) result from $m < 0$. Calculations were carried out with $m = \pm M$, $M > 0$. These spirals propagate in the

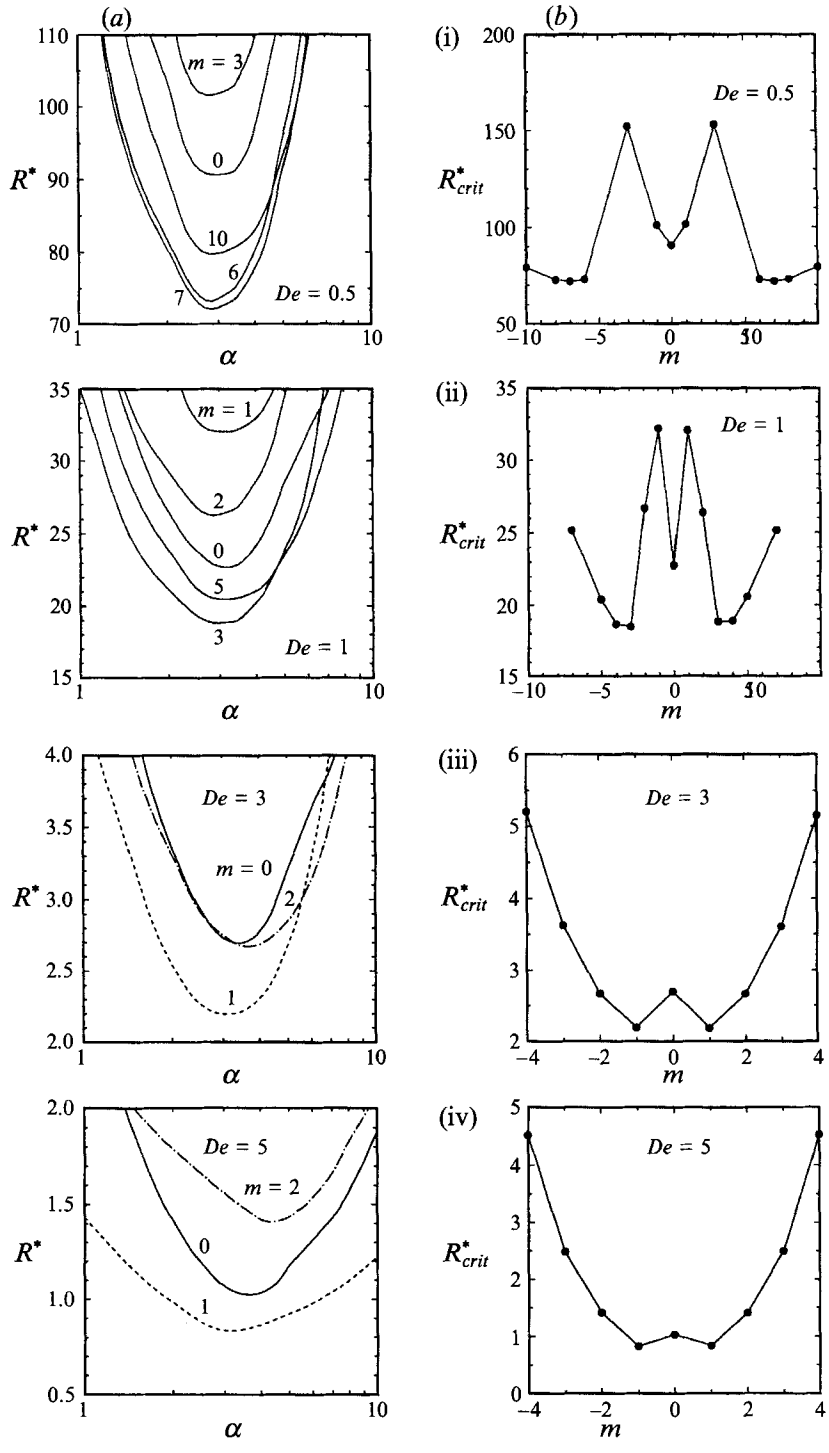

FIGURE 10. (*a*) The neutral stability curves $R^* = R^*(\alpha, m)$ and (*b*) $R^* = R^*_{crit}(\alpha_{crit}; m)$ computed for $\beta = 0.59$ and Deborah numbers of (i) 0.5, (ii) 1, (iii) 3 and (iv) 5.

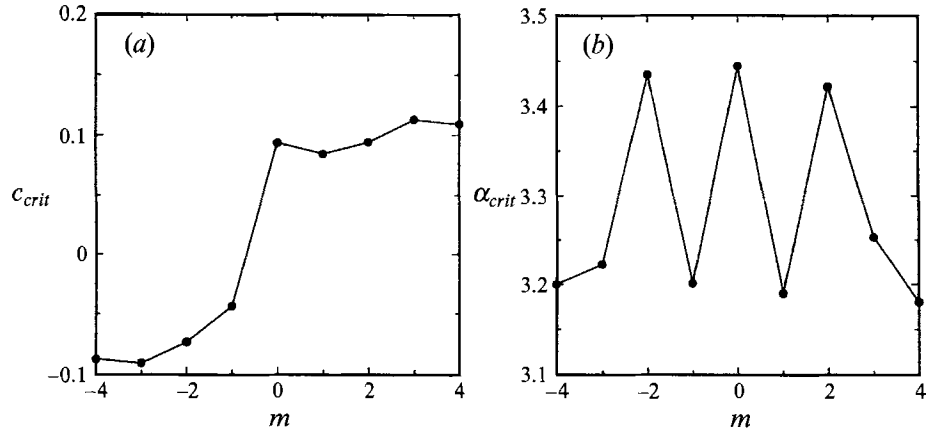

FIGURE 11. The critical (*a*) wave speed c_{crit} and (*b*) radial wavenumber α_{crit} as a function of m for $De = 3$ and $\beta = 0.59$.

direction normal to their surface with wave speed $c_n \equiv c/\cos(\epsilon) \equiv -\mathrm{Im}(\sigma)/(\alpha\cos(\epsilon))$, where c is the wave speed in the radial direction. Positive and negative values of c correspond to the spiral vortices travelling radially outward and inward, respectively.

The neutral stability curves $R^* = R^*(\alpha, m)$ computed with $\beta = 0.59$ and $0.5 \leqslant De \leqslant 5$ are shown in figure 10 for $-10 \leqslant m \leqslant 10$. The critical radii $R^* = R^*_{crit}(\alpha_{crit}, m)$ for the positive- and negative-angle spirals are approximately the same for all values of De. For $De = 0.5$, the lowest value of $R^* = R^*_{crit}(\alpha_{crit}, m)$ occurs for the azimuthal modes ($M = 7$) with the spiral angle $\epsilon = \pm 1.9°$. Another minimum in $R^* = R^*_{crit}(\alpha_{crit}, m)$ exists for the axisymmetric mode ($m = 0$). Increasing m from 0 to 4 increases the value of $R^* = R^*_{crit}(\alpha_{crit}, m)$. The dependence of R^*_{crit} on m is not monotonic, as shown in figures 10(*a*)(i) and 10(*b*)(i). The most dangerous radial wavenumbers are almost the same for all the modes. The critical modes for $De = 1$ are spiral vortices with $M = 5$, which corresponds to the angle $\epsilon = \pm 3.2°$. The critical radii $R^* = R^*_{crit}(\alpha_{crit}, m)$ do not depend monotonically on m and the most dangerous radial wavenumber varies only slightly with m, as shown in figures 10(*a*)(ii) and 10(*b*)(ii). For $De = 3$ and 5, the most dangerous mode is $m = 1$; however, the ordering of the non-axisymmetric ($m = 2$) and axisymmetric modes shifts with De. The $m = 2$ modes are more unstable than the $m = 0$ mode for $De = 3$; this ordering is reversed for $De = 5$. The most unstable radial wavenumber remains at approximately $\alpha = 3.5$ for all the disturbances shown in figures 10(iii) and 10(iv). The spiral angle for the most dangerous non-axisymmetric modes varies from 8° to 20° for De increasing from 3 to 5.

The critical radial wave speed $c = c_{crit}(\alpha_{crit}; m)$ and the most dangerous radial wavenumber $\alpha = \alpha_{crit}(m)$ are shown in figure 11 as a function of m for $De = 3$ and $\beta = 0.59$. The dynamics of the axisymmetric travelling vortices and the positive-angle spirals are different from those of negative-angle spirals. The positive-angle spirals and axisymmetric vortices travel radially outward, whereas negative-angle spirals travel radially inward, toward to the centre of the disk. The magnitude of the wave speed of the disturbances for negative- and positive-angle spirals remains almost constant at $c_{crit} = 0.1$, as shown in figure 11(*a*). The analysis was not continued to higher values of m because of inaccuracy in the eigenvalue calculations, as described above. The critical value of the radial wavenumber $\alpha_{crit}(m)$ is show in figure 11(*b*) as a function of m. The values for $m = \pm M$ are approximately the same and the wavenumbers are clustered in the range $3.2 \leqslant \alpha \leqslant 3.5$.

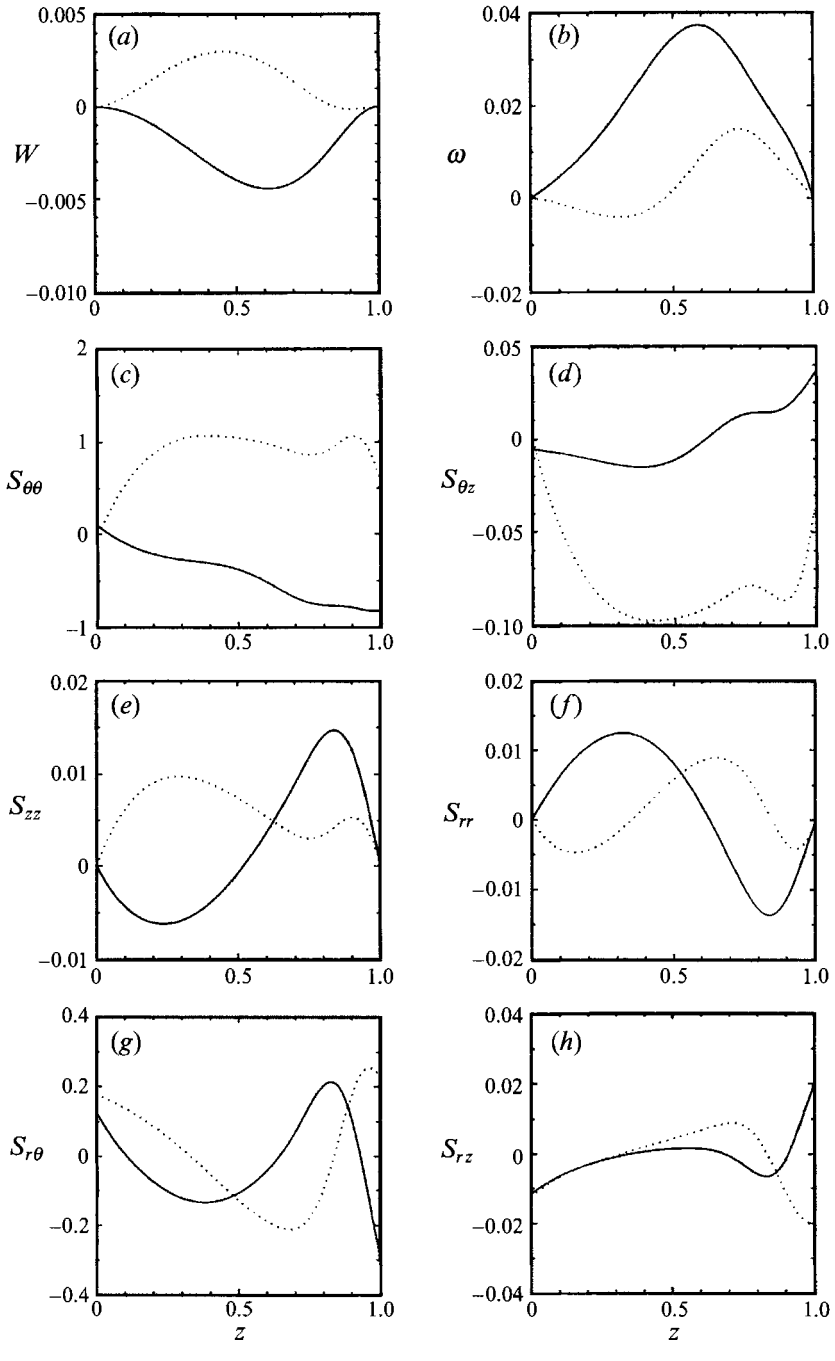

FIGURE 12. Disturbance amplitudes for Boger fluid ($\beta = 0.59$) shown as the plots of the real (solid curve) and imaginary (dotted curve) parts of (*a*) $W(z)$, (*b*) $\omega(z)$, (*c*) $S_{\theta\theta}$, (*d*) $S_{\theta z}$, (*e*) S_{zz}, (*f*) S_{rr}, (*g*) $S_{r\theta}$, and (*h*) S_{rz}. Plots are for $m = 1$, $R^* = 2.19$, $\beta = 0.59$ and $\alpha = 3.51$.

The vertical structure of the components of the eigenfunction corresponding to the vertical velocity, $\omega(z)$ and the components of the polymer part of the deviatoric stress are shown in figure 12 for the critical radius corresponding to $De = 3$, $\beta = 0.59$ and $m = 1$. Unlike the eigenfunctions of the axisymmetric disturbances, the non-

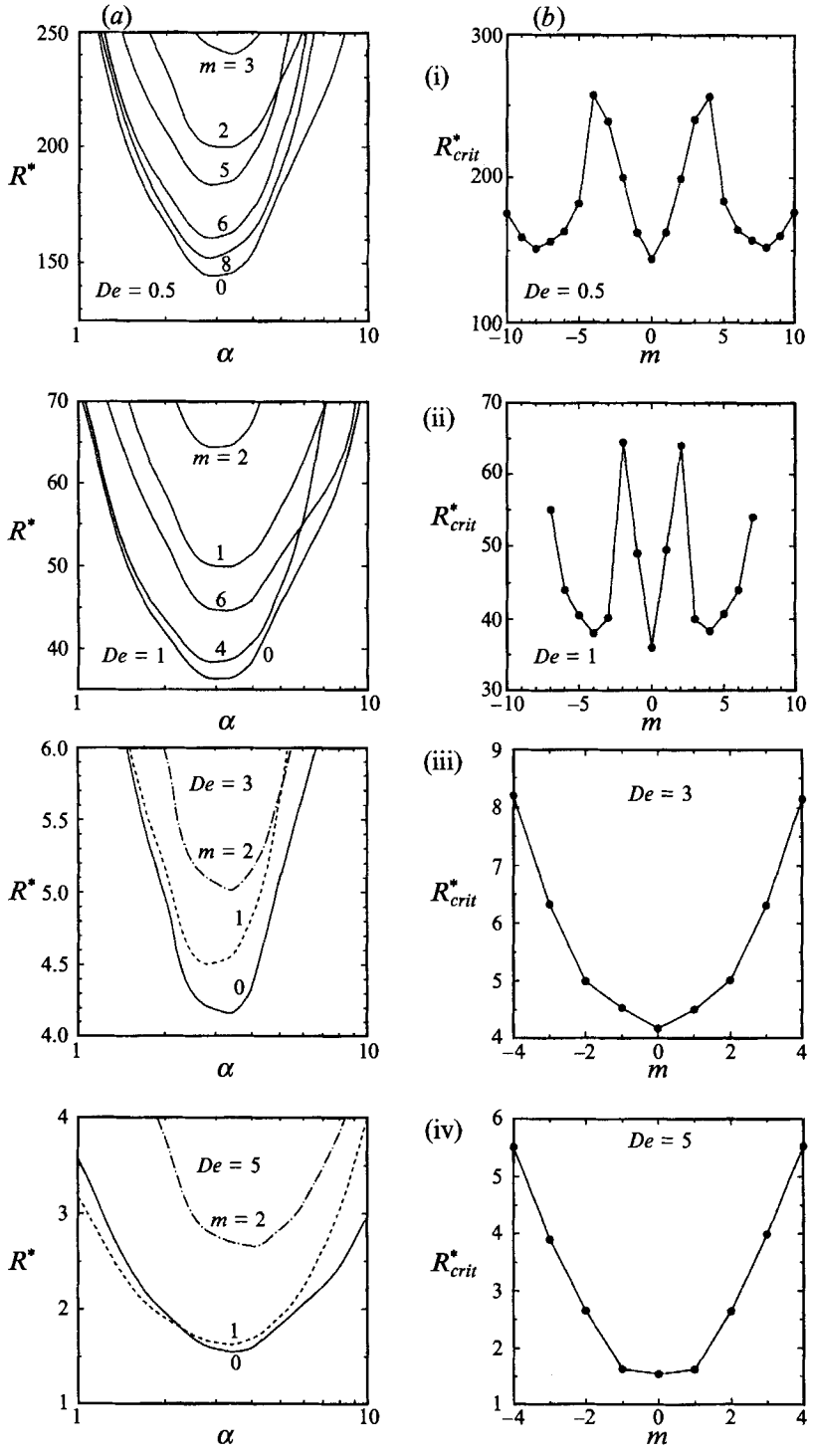

FIGURE 13. (*a*) The neutral stability curves $R^* = R^*(\alpha, m)$ and (*b*) $R^* = R^*_{crit}(\alpha_{crit}; m)$ computed for $\beta = 0.80$ and Deborah numbers of (i) 0.5, (ii) 1, (iii) 3 and (iv) 5.

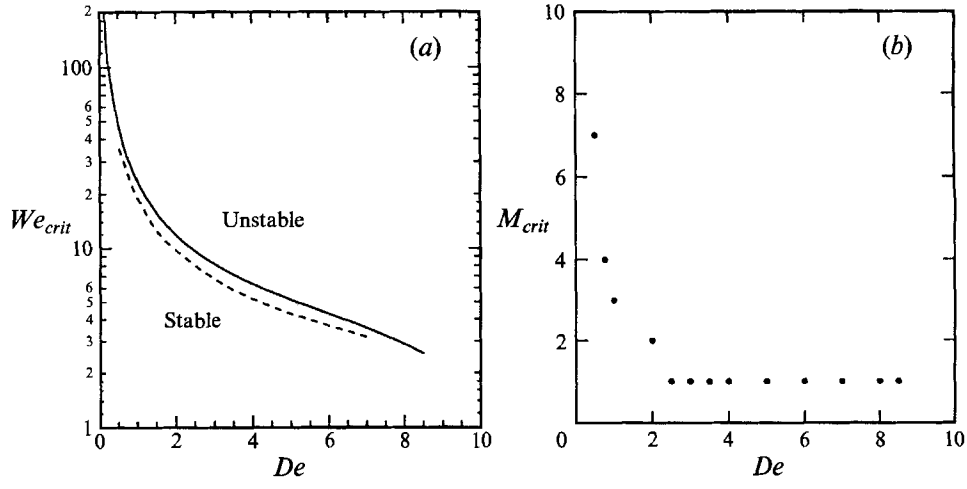

FIGURE 14. (*a*) The critical Weissenberg number $We_{crit}(De)$ for the onset of axisymmetric (——) and most dangerous non-axisymmetric (– – –) instabilities and (*b*) the most dangerous non-axisymmetric disturbance $M_{crit}(De)$ for $\beta = 0.59$.

axisymmetric functions do not have symmetry about the midplane $z = 0.5$. Both the vertical velocity and the vorticity have maxima closer to the stationary disk and have more structure than the most dangerous axisymmetric eigenfunction.

The dependence of the neutral stability curves $R^* = R^*_{crit}(\alpha_{crit}; m)$ on De is shown in figure 13 for $\beta = 0.80$, $0.5 \leqslant De \leqslant 5$, and $-10 \leqslant m \leqslant 10$. For all values De, the most dangerous mode is axisymmetric ($m = 0$). The critical radial wavenumber increases from 3 to 3.5 as De increases; however, it is weakly dependent on m. Note that the values of R^*_{crit} for the axisymmetric mode and the most dangerous non-axisymmetric mode are very close for all De, indicating that the axisymmetric instability and the spiral vortices will be observed almost simultaneously, as was the case for $\beta = 0.59$.

The critical value of the radius $R^* = R^*_{crit}(\alpha_{crit}; m)$ for $\beta = 0.59$ is plotted in figure 14(*a*) in terms of the Weissenberg number, defined by (3) as $We_{crit} \equiv De\, R^*_{crit}$, for the axisymmetric mode and the most dangerous non-axisymmetric disturbances. In figure 14(*a*), the onset radius R^*_{crit} for the most dangerous non-axisymmetric mode represents the outward-travelling spiral vortices ($m = +M$). The onset radius of the inward-travelling spirals is approximately the same. The axisymmetric disturbance is never the most dangerous; however, the difference in We_{crit} is small between the axisymmetric and the most dangerous non-axisymmetric modes. The value of $m = \pm M$ that corresponds to the most dangerous non-axisymmetric disturbance is shown in figure 14(*b*) as $M_{crit}(De)$. Note that M_{crit} increases as De is decreased, but the angle of the spiral ϵ goes to zero because R^*_{crit} approaches infinity in this limit. Similar results are predicted for the elastic Taylor–Couette flow, where Beris & Avgousti (1992) have shown that certain non-axisymmetric disturbances are more unstable than the axisymmetric disturbances.

4.2. *Upper-convected Maxwell (UCM) model*

Calculations for the upper-convected Maxwell fluid ($\beta = 0$) were carried out using the form (28) of the algebraic eigenvalue problem. The accuracy of the calculations was assessed by calculations of the entire spectrum of the algebraic eigenvalue problem for different polynomial discretizations for $De = 3$, $R^* = 5$, $m = 1$ and $\alpha = 3.5$; these

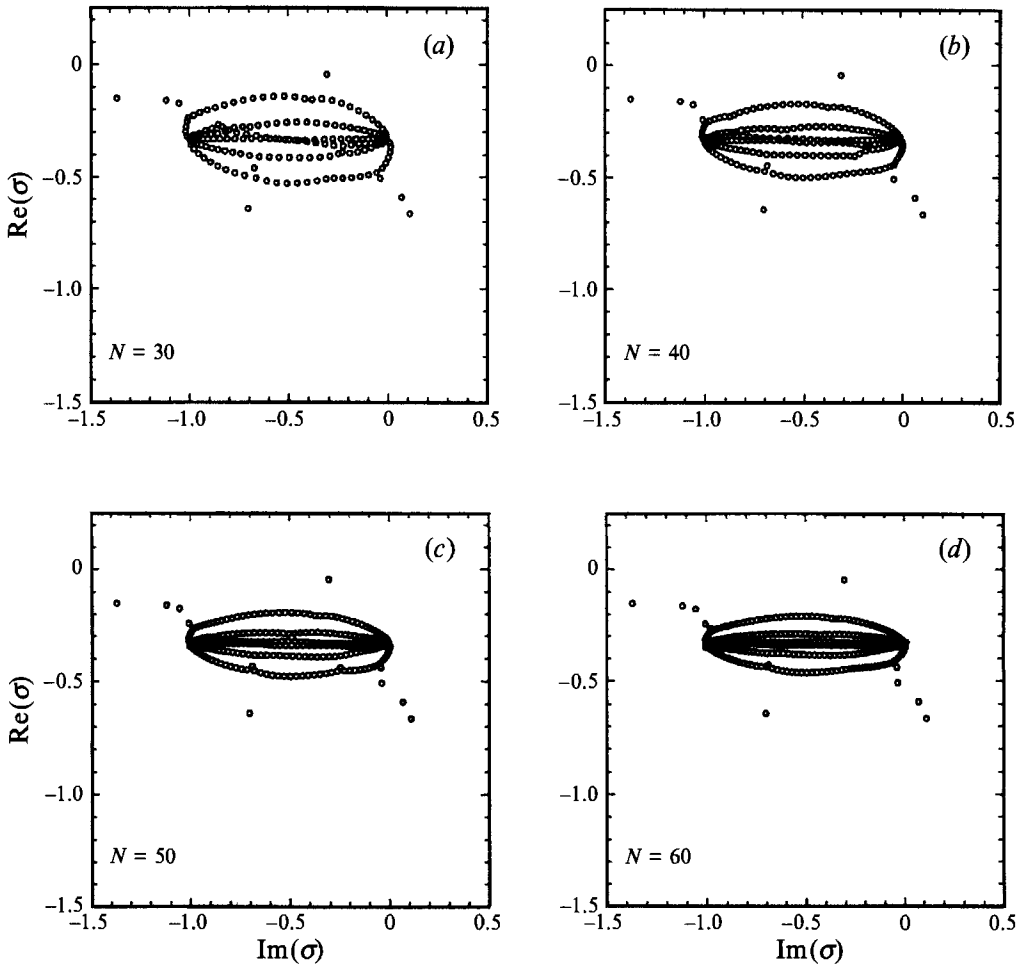

FIGURE 15. The spectra of the algebraic eigenvalue problem computed for upper-convected Maxwell fluid ($\beta = 0$), $m = 1$, $\alpha = 3.5$, $R^* = 5$, $De = 3$, with the discretization using (*a*) $N = 30$, (*b*) 40, (*c*) 50 and (*d*) 60.

spectra are shown in figure 15. Each shows six branches of a continuous spectrum and discrete eigenvalues. The real parts of the discrete spectra are connected at a point where $\mathrm{Re}(\sigma) = -1/De$ and the imaginary parts are 0 and $-m$. These six branches seem to correspond to the upper six branches that were seen for the calculations with the Oldroyd-B model. The instability corresponds to a discrete eigenvalue having $\mathrm{Re}(\sigma) > 0$. As was the case for the Oldroyd-B model, the computation of the continuous spectrum was much more difficult than the discrete spectrum; much more highly resolved discretizations ($N \gg 1$) were required for accuracy. Figure 16 demonstrates the convergence with increasing N of the most unstable component of the discrete spectrum; this eigenvalue is converged to at least one part in 10^4 with $N = 10$ for $0 \leqslant m \leqslant 2$ and $N = 25$ for $m = 3$, whereas the eigenvalues for the most unstable component of the continuous spectrum were not converged to this accuracy with $N = 60$. Again the behaviour with increasing N suggests that $\mathrm{Re}(\sigma)$ for eigenvalues in the continuous spectrum converges to $-1/De$ for all values of m, as was the case for the Oldroyd-B fluid.

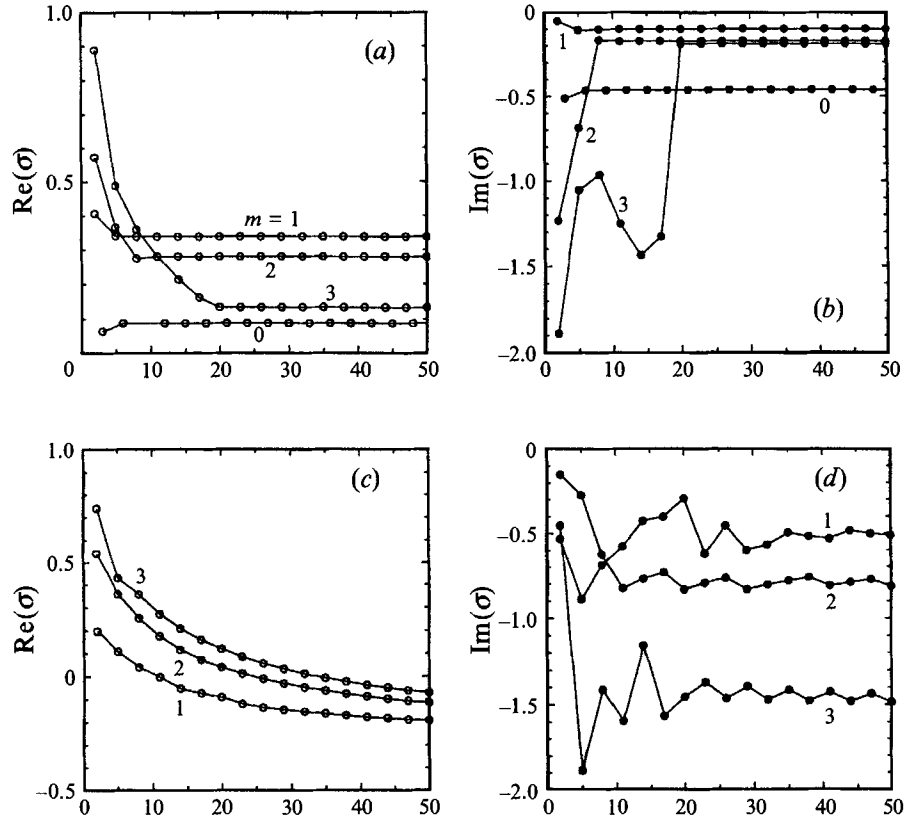

FIGURE 16. The spectral convergence of the least-stable eigenvalues for $\alpha = 3.5$, $R^* = 5$, $\beta = 0$, $De = 3$ and $1 \leqslant m \leqslant 3$, shown as plots of (*a*) the real and (*b*) imaginary parts of the most unstable eigenvalue of the discrete spectrum, and (*c*) the real and (*d*) imaginary parts of the most unstable eigenvalue of the continuous spectrum as a function of discretization N.

The neutral stability curves $R^* = R^*(\alpha; m)$ for several values of m and the dependence of the critical radial locations $R^* = R^*_{crit}(\alpha_{crit}; m)$ on m are shown in figure 17 for $0.5 \leqslant De \leqslant 5$. For the UCM model, the difference in R^*_{crit} is substantial between the axisymmetric and the most dangerous non-axisymmetric modes, indicating that spiral vortices should be seen significantly before the axisymmetric instability. Also, the spiral angle of the vortices increases from 3.2° to 35° as De increases from 0.5 to 5.

The critical value of the radius $R^* = R^*_{crit}(\alpha_{crit}; m)$ is shown in figure 18(*a*) in terms of the Weissenberg number, defined by (3) as a function of De, for the axisymmetric mode and the most dangerous non-axisymmetric mode. The predictions for these two types of disturbance diverge for small De and converge for $De \gg 1$; the axisymmetric disturbance is never the most dangerous. The value of $m = \pm M$ that corresponds to the most dangerous non-axisymmetric disturbance is shown in figure 18(*b*) as $M_{crit}(De)$.

5. Comparison with experiments of McKinley *et al.*

The predictions for the onset of the instability described above are compared directly with the observations of McKinley *et al.* (1991) for the instability of a PIB/PB/C14 Boger fluid. For this comparison we consider the Boger fluid as an Oldroyd-B fluid with $\beta = 0.59$, as determined directly for measurement of the solvent viscosity and the

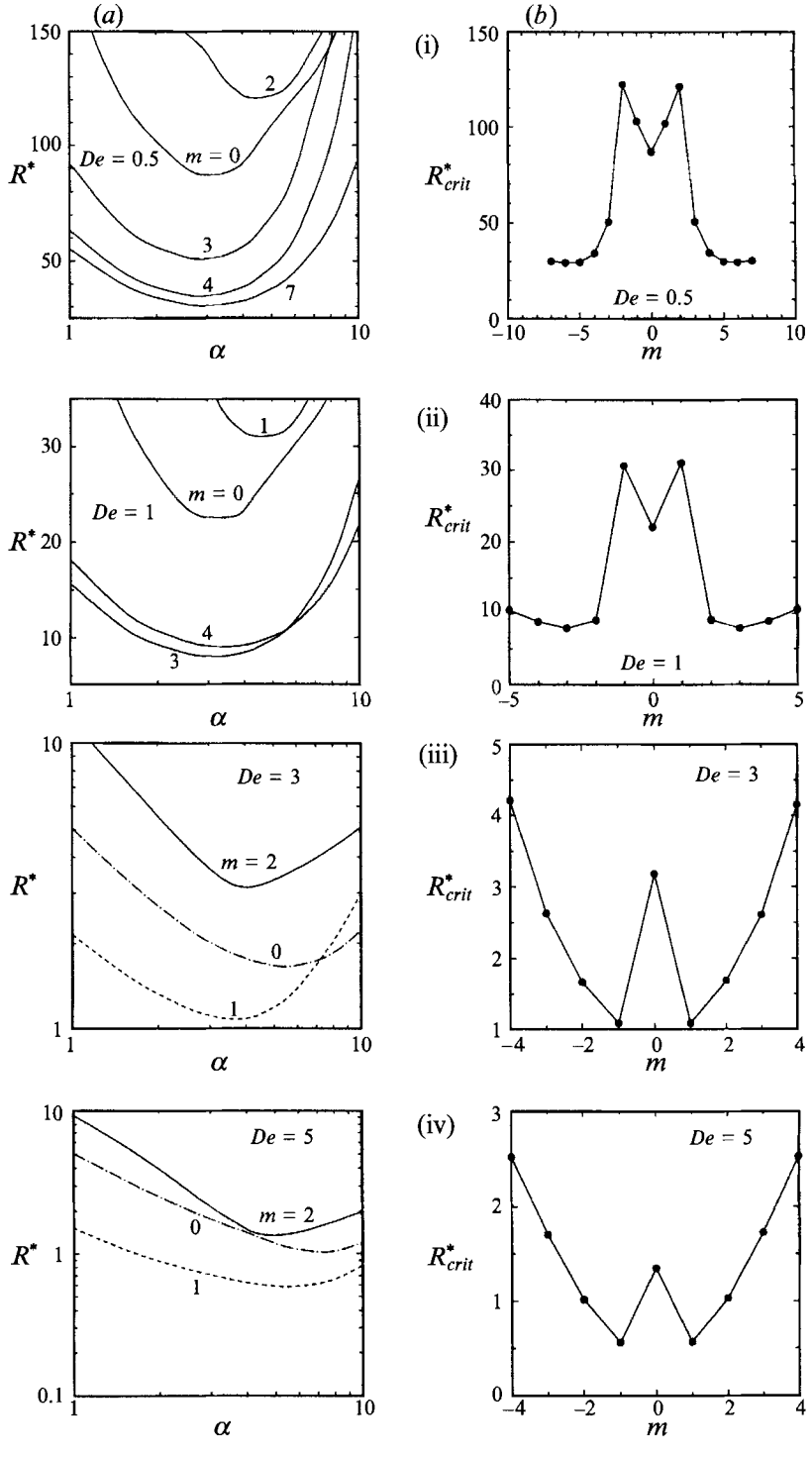

FIGURE 17. (*a*) The neutral stability curves $R^* = R^*(\alpha, m)$ and (*b*) $R^* = R^*_{crit}(\alpha_{crit}; m)$ computed for $\beta = 0$ and Deborah numbers of (i) 0.5, (ii) 1, (iii) 3 and (iv) 5.

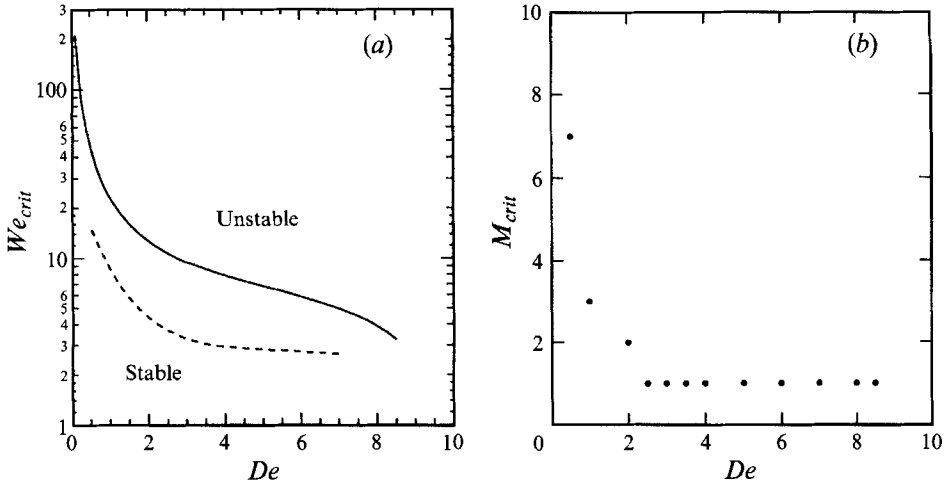

FIGURE 18. (*a*) The critical Weissenberg number $We_{crit}(De)$ for the onset of axisymmetric (——) and most dangerous non-axisymmetric (– – –) instabilities and (*b*) the most dangerous non-axisymmetric disturbance $M_{crit}(De)$ for $\beta = 0$.

almost constant viscosity of the Boger fluid. The shear thinning of the Boger fluid is included in this characterization by using the shear-thinning relaxation time defined by (6) which was the definition of shear rate $\dot{\gamma} \equiv \Omega R/H$ that corresponds to the shear rate of the viscometric flow at the dimensional radial position $\hat{r} = R^*H$ for the disturbance.

Formally, modelling a Boger fluid as a generalized Oldroyd-B fluid with a viscosity and a relaxation time that depend on shear rate, $\lambda = \lambda(\dot{\gamma})$, would include incorporation of the effect of the shear-rate-dependent relaxation time into the equations for the disturbance in the stress field formed from the linearized constitutive equation and the modification of the stress field of the base state. These changes will modify the stability results described in §4. Our approach of modifying the time constant does not take these changes into account and is an *ad hoc* method for including the shear thinning of the fluid. However, because the instabilities described by the analysis are localized at a specific radial location and because the shear rate varies monotonically with radius, using the definition of the local shear rate to determine the relaxation time seems justified.

The data of McKinley *et al.* for the onset of the instability are shown in figure 19 by sets of points in $We = We_{crit}(De)$ which correspond to measurements with different gaps between the disks, i.e. different values of R/H for the disks. The onset of small-scale vortices that travel inward from the outer edge of the disk is marked by the change from open (○) to solid (●) circles. The predictions from the linear stability analysis for the axisymmetric and most dangerous non-axisymmetric modes are shown for comparison. The agreement between experiment and theory for the prediction of the onset of the instability is good. It is interesting to note that the differences between axisymmetric and non-axisymmetric modes are so small that distinguishing these modes by experiments may be extremely difficult. Indeed, the visualization of the nonlinear state by McKinley *et al.* showed both axisymmetric and non-axisymmetric spiral modes.

Both the axisymmetric and non-axisymmetric modes correspond to critical radial wavenumbers of approximately $\alpha_{crit} = 3.2$, which gives a secondary roll cell with lengthscale of approximately twice the gap width or $2H$. Taking the stripes in the video

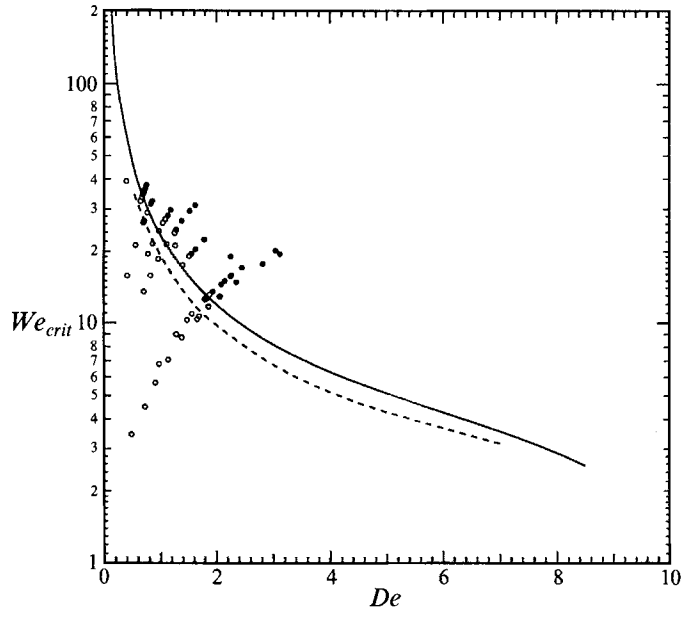

FIGURE 19. The critical Weissenberg number $We_{crit}(De)$ for the onset of axisymmetric (solid curve) and most dangerous non-axisymmetric (dashed curve) disturbances predicted by stability analysis and the stable (○) and unstable (●) viscometric flow observed by McKinley *et al.* (1991); calculations are for the Oldroyd-B fluid with $\beta = 0.59$.

of McKinley *et al.* (1991) to correspond to two secondary roll cells gives an approximate spacing from the experiments as $2H$. This surprising agreement is discussed in §6.

The wave speed for $De = 4.65$ predicted from the linear analysis is $c_{crit} = 0.063$ for the axisymmetric mode and $c_{crit} = 0.055$ and -0.072 for $m = +1$ and -1 non-axisymmetric modes, respectively. Although travelling wave moving radially outward from near the centre of the disk and inward from the outer edge of the disks were observed in the experiments of McKinley *et al.*, no attempt was made to measure directly the wave speed. For the same De, the power spectrum of the shear stress measured by McKinley *et al.* in a commercial rheometer showed a weak peak at frequency $f = 0.025$ Hz and a number of other peaks ranging between $0.045 \leqslant f \leqslant 1.4$ Hz. The appearance of these peaks is in reasonable agreement with the frequencies predicted by linear stability analysis of $f = 0.037$ for the axisymmetric mode and $f = 0.032$ for the $m = 1$ non-axisymmetric mode.

6. Mechanism of instability

The micromechanical mechanism for the instability in the flow between the parallel rotating disks can be described by referring to the development of the Oldroyd-B model from the kinetic theory for a dilute solution of infinitely extensible dumbbells (Bird *et al.* 1987*b*), and by using an argument similar to the one developed by Larson *et al.* (1990) and Joo & Shaqfeh (1992). Here the polymeric stress is proportional to the ensemble average of the dumbbell confirmation; hence S_{zz} is a measure of the stretching of the dumbbells in the z-direction.

The mechanism of the instability in the axisymmetric mode is associated with the coupling between the disturbance, base-state polymeric stress and the velocity gradient

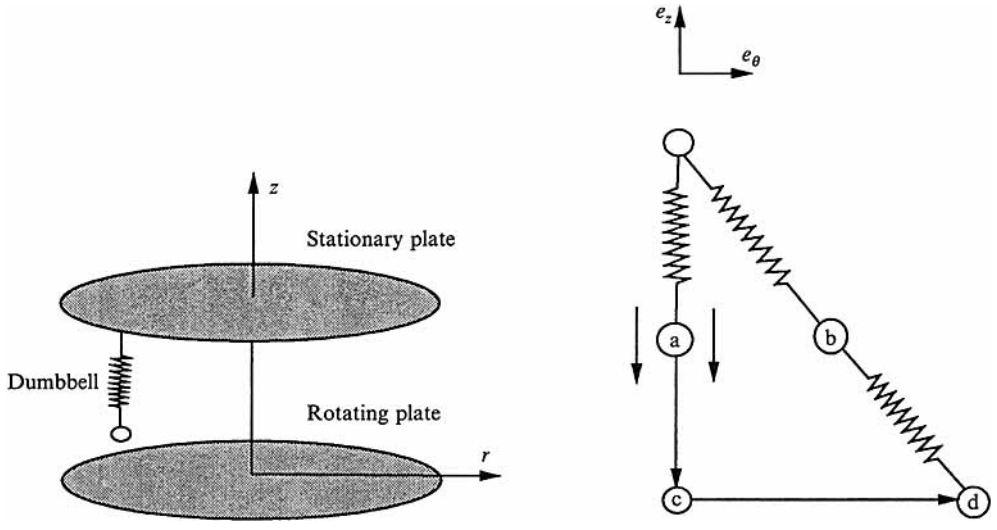

FIGURE 20. Schematic of a dumbbell located in the axial direction between the plates. The base flow stretches the dumbbell in the azimuthal direction from (a) to (b); secondary flow deflects the bead in the axial direction; and the base flow stretches the bead farther from (c) to (d).

in the z-direction, which couples through the curved streamlines of the base flow to create a perturbation in the hoop stress, $S_{\theta\theta}$, that reinforces the secondary flow. To see this consider an axisymmetric disturbance, which gives rise to an axial extensional component of the velocity gradient $\partial u_z/\partial z$ and which stretches the dumbbell in the z-direction, as shown in figure 20. That disturbances creates a perturbation to the normal stress S_{zz} which must satisfy

$$\mathrm{L}(S_{zz}) = 2\beta_p \frac{\partial u_z}{\partial z}. \tag{29a}$$

The coupling between the perturbation in the axial normal stress S_{zz}, the base-state velocity gradient $\partial u_{0z}/\partial z$, shear stress $S_{0\theta z}$ and the perturbation to the velocity gradient $\partial u_z/\partial z$ produces a perturbation to the shear stress given by

$$\mathrm{L}(S_{\theta z}) + De\, r S_{zz} + \beta_p De\, r \frac{\partial u_z}{\partial z} = 0. \tag{29b}$$

The coupling between the perturbation shear stress and the base-state velocity gradient deforms the dumbbell in the azimuthal direction which causes an increase in the 'hoop stress' $S_{\theta\theta}$

$$\mathrm{L}(S_{\theta\theta}) + 2De\, r S_{\theta z} = 0. \tag{29c}$$

Because the streamlines are curved, the elastic hoop stress reinforces the axial perturbation flow. Taking the essential terms in the radial and axial momentum equations, (16a) and (16c) become

$$\frac{S_{\theta\theta}}{r} - \frac{\partial p}{\partial r} + \beta \nabla^2 u_r = 0, \tag{29d}$$

$$-\frac{\partial p}{\partial z} + \beta \nabla^2 u_z = 0. \tag{29e}$$

Assuming that the disturbance is localized in r, we write the disturbance in the Fourier

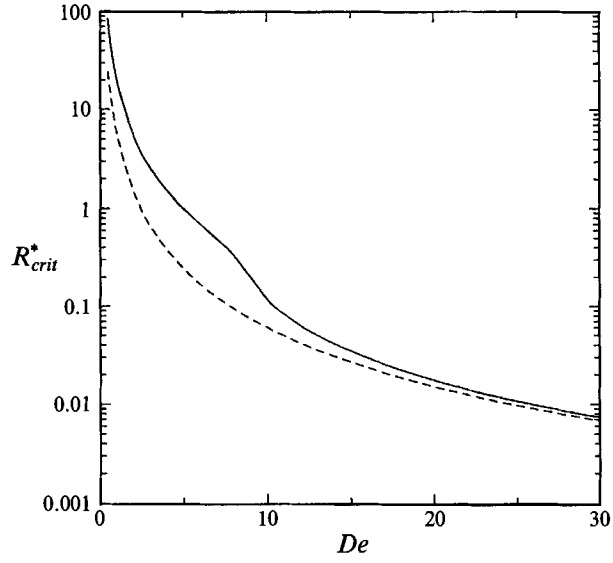

FIGURE 21. The critical dimensionless radius or aspect ratio $R^* = R^*_{crit}(\alpha_{crit})$ computed for $\beta = 0.50$ and Deborah numbers for the onset of axisymmetric instability. The solid and dashed curves are for the full eigenvalue problems, (19) and (20), and for the approximate analysis that leads to (30), respectively.

form $\exp(i\alpha r + \sigma t)$. Using continuity, $i\alpha U = -DW$, and eliminating pressure and stress components from 29(*a–e*) yields the fourth-order equation

$$P^3\beta(D^4 - 2\alpha^2 D^2 + \alpha^4)\, W + P2i\, De^2\, R^*\alpha\beta_p\, D^2 W + 4\, De^2\, R^* i\alpha\beta_p\, D^2 W = 0, \quad (30)$$

where $P \equiv (1 + De\,\sigma)$. Equation (30) with boundary conditions (21) describes an eigenvalue problem that can be solved using the numerical technique described in §3. The critical value of the radius $R^* = R^*_{crit}(\alpha_{crit})$ for the onset of the axisymmetric instability computed from this equation is plotted as a function of *De* in figure 21. The solution of the full eigenvalue problem is shown as well; the predictions of the two analyses are in reasonable agreement. The difference in R^*_{crit} is substantial for small values of Deborah number because of the contributions from the terms neglected in (19) and (20). However, both curves approach the same asymptote for large values of *De*, indicating that the mechanism described above is operative in the full analysis as well.

The mechanism for the non-axisymmetric modes requires a different pathway to the development of the 'hoop stress' $S_{\theta\theta}$. The perturbation of normal shear stress S_{zz} is created from both vertical and azimuthal gradients of the perturbation axial velocity. The couplings of S_{zz}, $\partial u_{0\theta}/\partial z$, $\partial u_z/\partial\theta$, $S_{0\theta\theta}$, $\partial u_z/\partial z$ and $S_{0\theta z}$ produce the perturbation shear stress. The hoop stress is generated from the coupling of the perturbation to the shear stress and the base-state velocity gradient $\partial u_{0\theta}/\partial z$. The dumbbell is stretched in the axial direction by both azimuthal and axial variations in the perturbation to the vertical velocity.

7. Discussion

The analysis of the linear stability problem defined for radially localized disturbances to the viscometric flow between two parallel rotating disks leads to a picture for the onset of the viscoelastic flow instability that is consistent with many of the observations

of McKinley *et al.* (1991). For given Deborah number and viscosity ratio in the Oldroyd-B model, instability begins at a critical radius and has the form of either axisymmetric or spiral vortices that move radially outward and inward as travelling waves. Both the axisymmetric and spiral modes can cause instability at approximately the same values of radial wavenumber and radial location, depending on De and the viscosity ratio. In some cases several modes have onset close enough in radial location to be indistinguishable in experiments. The radial location for the onset of the instability decreases with increasing De.

The results of this analysis are compared directly to the experiments of McKinley *et al.*, by assuming that the instability starts at the outer radius of the finite disks in the experiment and defining both the Deborah and Weissenberg numbers according to (3). The comparison of the predictions for the Oldroyd-B fluid with the appropriate viscosity ratio to the experimental measurements for $We = We_{crit}(De)$ is good, as shown in figure 19. These results strongly suggest that the radial instability described here is responsible for the anti-thixotropic transition seen in rotating-disk rheometers. The flow instability has obvious and important implications for the use of a parallel-disk apparatus to measure the rheological properties of very elastic fluids, by rendering the assumption of a known viscometric fluid invalid beyond a critical value of De, which can be ascertained from the results included here. The same type of instability also is responsible for the flow transitions documented by McKinley *et al.* in a cone and plate rheometer; we will report an analysis of this instability in a later paper.

The analysis described here cannot be compared to Phan-Thien's analysis (1983, 1985) in any limit. The plot of $We = We_{crit}(De)$ shown in figure 19 indicates that R^* tends to infinity at $De = 0$, but not at a finite value of De. Hence, a finite value of the critical onset radius is predicted for any finite value of Deborah number. However, the stability analysis of Phan-Thien predicts that there exists finite value of the critical Deborah number below which the viscometric motion is stable everywhere. The instability predicted by Phan-Thien is in the similarity form so the resulting secondary flow consists of one cell in the radial direction, which is equivalent to our disturbance form when the wavelength in the radial direction is infinite. This limit is approached for large values of Deborah number for which the critical aspect ratio and the critical wavenumber asymptote to zero; see figure 21. Because the present analysis is limited to the localized disturbance, the prediction in this limit is not reliable.

Other points of comparison between the experiments of McKinley *et al.* and the calculations reported here appear to require nonlinear analysis. First, the propagation of the travelling waves to radial locations satisfying $r < R^*$ would seem to correspond to motion of the instability into a region of the disk that is otherwise stable to the linear instability. Indeed the nonlinear evolution of the instability is shown by McKinley *et al.* to be initially subcritical, i.e. there is a region of De of hysteresis where the viscometric and nonlinear states coexist. The long development time and the complex spectrum of the time dependence of the torque induced by the nonlinear flow suggest that the nonlinear state that evolves after the subcritical instability is an almost chaotic interaction of several nonlinear modes, perhaps including another instability that begins at the centre of the disk. It might be coincidence that the apparent spatial wavelength of this nonlinear state and the wavelength of the radial travelling wave agree; the value of the nonlinear state is approximately $2H$, and the values predicted by the linear stability analysis vary around $2H$. Understanding of the evolution and interactions of different travelling instability modes requires weakly nonlinear analysis and full nonlinear simulations.

Although the analysis is restricted to radially localized disturbances, it still includes

the effects of streamline curvature through the base flow and terms retained in the linear stability analysis. The discussion in §6 shows that this effect is the most important component of the instability mechanism. The different stability properties of positive ($m > 0$) and negative ($m < 0$) angle spirals are a result of this curvilinear effect. The analysis predicts that negative- and positive-angle spirals onset at approximately the same radial position, so it is expected to be difficult to distinguish these disturbances. Interestingly, both inward- and outward-travelling spirals were observed by McKinley *et al.* (1991). The experimental observation of the onset of the instability as a subcritical transition suggests that a nonlinear analysis is needed to predict the interaction between these modes that are observed for *De* above criticality.

Although the analysis described here gives reasonable agreement with previous experimental observations, there are a number of theoretical questions that still need to be considered, even for linear stability theory. The analysis described here is based on the assumption of radially localized disturbances. This assumption greatly simplifies the analysis, but has the drawback of making disturbances appear approximately rectilinear and not accounting for the finiteness of the disks or the importance of the centreline. Asymptotic expansions in r, as applied by Malik *et al.* (1981), Malik (1986), and Öztekin *et al.* (1992), begin to alleviate the first limitation, but still will not be valid near the centreline or disk edge. Full solution of the full three-dimensional eigenvalue problem appears to be the only method for addressing this problem in general.

As described above, the method discussed in §5 for incorporating shear thinning is approximate, at best. A rigorous linear stability analysis incorporating shear thinning into the constitutive equation is needed to justify this approximation.

This research was partially supported by the Fluid Mechanics and Hydraulics Program of the National Science Foundation. We are grateful to G. H. McKinley and J. A. Byars for many helpful discussions of their experiments.

REFERENCES

BERIS, A. N. & AVGOUSTI, M. 1992 Viscoelastic flow instabilities: inception and non-linear evolution. In *Theoretical and Applied Rheology. Proc. Xth Intl Cong. on Rheology, Belgium* (ed. P. Modenaers & R. Keunings), vol. 1, pp. 33–38. Elsevier.

BINNINGTON, R. J. & BOGER, D. V. 1986 Remarks on non-shear thinning elastic fluids. *Polymer Engng Sci.* **26**, 133–138.

BIRD, R. B., ARMSTRONG, R. C. & HASSAGER, O. 1987*a* *Dynamics of Polymeric Liquids, Vol. 1, Fluid Mechanics*, 2nd edn. Wiley-Interscience.

BIRD, R. B., CURTISS, C. F., ARMSTRONG, R. C. & HASSAGER, O. 1987*b* *Dynamics of Polymeric Liquids, Vol. 2, Kinetic Theory*, 2nd edn. Wiley-Interscience.

BROWN, R. A., SZADY, M. J., NORTHEY, P. J. & ARMSTRONG, R. C. 1993 On the numerical stability of mixed finite element methods for viscoelastic flows governed by differential constitutive equations. *J. Theor. Comput. Fluid Dyn.* (in press).

GRIFFITHS, D. F., JONES, D. T. & WALTERS, K. 1969 A flow reversal due to edge effects. *J. Fluid Mech.* **36**, 161–175.

GORODSTOV, V. A. & LEONOV, A. I. 1967 On a linear stability of a plane parallel Couette flow of viscoelastic fluid. *Z. Angew. Math. Mech.* **31**, 310–319.

HILL, C. T. 1972 Nearly viscometric flow in the disk and cylinder systems II. Experimental. *Trans. Soc. Rheol.* **16**, 213–245.

JACKSON, J. P., WALTERS, K. & WILLIAMS, R. W. 1984 A rheometrical study of Boger fluids. *J. Non-Newtonian Fluid Mech.* **14**, 173–188.

JOO, Y. L. & SHAQFEH, E. S. G. 1992 A purely elastic instability in Dean and Taylor–Dean flow. *Phys. Fluids* A **4**, 524–543.

LARSON, R. G. 1992 Instabilities in viscoelastic flows. *Rheologica Acta* **31**, 213–263.

LARSON, R. G., SHAQFEH, E. S. G. & MULLER, S. J. 1990 A purely elastic instability in Taylor–Couette flow. *J. Fluid Mech.* **218**, 573–600.

LAUN, H. M. & HINGMANN, R. 1990 Rheological characterization of the fluid M1 and of its components. *J. Non-Newtonian Fluid Mech.* **35**, 137–157.

MAGDA, J. J. & LARSON, R. G. 1988 A transition in ideal elastic liquids during shear flow. *J. Non-Newtonian Fluid Mech.* **30**, 1–19.

MALIK, M. R. 1986 The neutral curve for stationary disturbances in rotating disk flow. *J. Fluid Mech.* **164**, 275–287.

MALIK, M. R., WILKINSON, S. P. & ORSZAG, S. A. 1981 Instability and transition in rotating disk flow. *AIAA J.* **19**, 1131–1138.

MCKINLEY, G. H., BYARS, J. A., BROWN, R. A. & ARMSTRONG, R. C. 1991 Observations on the elastic instability in cone-and-plate and parallel-plate flows of a polyisobutylene Boger fluid. *J. Non-Newtonian Fluid Mech.* **40**, 201–229.

NORTHEY, P., ARMSTRONG, R. C. & BROWN, R. A. 1990 Finite-element calculation of time dependent, two dimensional inertial flows in circular Couette flow. *Annual AIChE Meeting, November, 1990, Paper* 167j.

NORTHEY, P., ARMSTRONG, R. C. & BROWN, R. A. 1992 Finite-amplitude time-periodic states in viscoelastic Taylor–Couette flow described by the UCM model. *J. Non-Newtonian Fluid Mech.* **42**, 117–139.

ÖZTEKIN, A., BORNSIDE, D. E. & BROWN, R. A. 1993 Stability of forced flow over a rotating disk. Unpublished.

PHAN-THIEN, N. 1983 Coaxial-disk flow of an Oldroyd-B fluid, exact solution and stability. *J. Non-Newtonian Fluid Mech.* **13**, 325–340.

PHAN-THIEN, N. 1985 Cone-and-plate flow of the Oldroyd-B fluid is unstable. *J. Non-Newtonian Fluid Mech.* **13**, 325–340.

QUINZANI, L. M., MCKINLEY, G. H., BROWN, R. A. & ARMSTRONG, R. C. 1991 Modelling the rheology of polyisobutylene solutions. *J. Rheol.* **34**, 705–748.

SHAQFEH, E. S. G., MULLER, S. J. & LARSON, R. G. 1992 The effects of gap width and dilute solution properties on the viscoelastic Taylor–Couette instability. *J. Fluid Mech.* **235**, 285–317.

STEIERT, P. & WOLFF, C. 1990 Rheological properties of a polyisobutylene in a kerosene/polybutene mixture in simple shear flow. *J. Non-Newtonian Fluid Mech.* **35**, 189–196.

WILKINSON, S. P. & MALIK, M. R. 1983 Stability experiments in the flow over a rotating disk. *AIAA Paper* 83–1760.

ZEBIB, A. 1987 Removal of spurious modes encountered in solving stability problems by spectral methods. *J. Comput. Phys.* **70**, 521–525.